

## THE CHEMICALLY CONTROLLED SYNTHESIS OF DUST IN TYPE II-P SUPERNOVAE

ARKAPRABHA SARANGI AND ISABELLE CHERCHNEFF

Departement Physik, Universität Basel, CH-4056 Basel, Switzerland

arkaprabha.sarangi@unibas.ch, isabelle.cherchneff@unibas.ch

Received 2013 April 5; accepted 2013 August 16; published 2013 October 4

### ABSTRACT

We study the formation of molecules and dust clusters in the ejecta of solar metallicity, Type II-P supernovae (SNe) using a chemical kinetic approach. We follow the evolution of molecules and small dust cluster masses from day 100 to day 1500 after explosion. We consider stellar progenitors with initial masses of 12, 15, 19, and 25  $M_{\odot}$  that explode as SNe with stratified ejecta. The molecular precursors to dust grains comprise molecular chains, rings and small clusters of silica, silicates, metal oxides, sulfides and carbides, pure metals, and carbon, where the nucleation of silicate clusters is described by a two-step process of metal and oxygen addition. We study the impact of the  $^{56}\text{Ni}$  mass on the type and amount of synthesized dust. We predict that large masses of molecules including CO, SiO, SiS,  $\text{O}_2$ , and SO form in the ejecta. We show that the discrepancy between the small dust masses detected at infrared wavelengths some 500 days post-explosion and the larger amounts of dust recently detected with *Herschel* in SN remnants can be explained by the non-equilibrium chemistry linked to the formation of molecules and dust clusters in the ejected material. Dust gradually builds up from small ( $\sim 10^{-5} M_{\odot}$ ) to large masses ( $\sim 5 \times 10^{-2} M_{\odot}$ ) over a 5 yr period after explosion. Subsequent dust formation and/or growth is hampered by the shortage of chemical agents participating in the dust nucleation and the long timescale for accretion. The results highlight the dependence of the dust chemical composition and mass on the amount of  $^{56}\text{Ni}$  synthesized during the explosion. This dependence may partly explain the diversity of epochs at which dust forms in SNe. More generally, our results indicate that Type II-P SNe are efficient but moderate dust producers with an upper limit on the mass of synthesized dust ranging from  $\sim 0.03$  to  $0.09 M_{\odot}$ . Other dust sources must then operate at high redshift to explain the large quantities of dust present in young galaxies in the early universe.

**Key words:** astrochemistry – dust, extinction – ISM: supernova remnants – molecular processes – supernovae: general

*Online-only material:* color figures

### 1. INTRODUCTION

Stars with an initial mass on the main sequence comprised between 8  $M_{\odot}$  and 30  $M_{\odot}$  usually end their life as core-collapse Type II-P supernovae (SNe). Despite the huge amount of energy released by the explosion ( $\sim 1 \times 10^{51}$  erg) and the harsh physical conditions that characterize the ejected stellar gas (hereafter referred as the ejecta), dust and molecules have been detected in many SNe a few hundred days after the explosive event. The first evidence for dust synthesis in SN ejecta was provided by the explosion of SN1987A in the Large Magellanic Cloud more than 25 years ago. The extensive observational coverage of the event at mid-infrared (IR) wavelengths allowed the detection of the fundamental and overtone transitions of a few molecules, specifically carbon monoxide, CO, and silicon monoxide, SiO, as early as  $\sim 120$  days post-explosion. The observations also highlighted the formation of dust grains after day 400 (Spyromilio et al. 1988; Lucy et al. 1989; Meikle et al. 1989; Moseley et al. 1989; Roche et al. 1991; Danziger et al. 1991; Wooden et al. 1993).

Since then, warm dust has been detected in several SNe (e.g., Elmhamdi et al. 2003b; Kotak et al. 2005, 2006, 2009; Sugerman et al. 2006; Inserra et al. 2011b; Gallagher et al. 2012). An excess in the mid-IR, combined with a decrease of several magnitudes in the optical light curve and blueshifted emission lines, are the usual indicators of the synthesis of dust in the ejecta. The fundamental band of SiO has been detected in a few SNe, e.g., SN2004et, and the gradual fading of the transition over time was ascribed to the depletion of SiO in the condensation process of

dust grains in the ejecta  $\sim 400$  days post-outburst (Kotak et al. 2009). Most important are the small amounts of warm dust derived from modeling the mid-IR excess in SNe with masses that range from  $1 \times 10^{-5} M_{\odot}$  to  $1 \times 10^{-3} M_{\odot}$ . These values are usually derived assuming a homogenous ejecta and a mixture of silicates and carbon, the prevalent types of dust in galaxies, while other condensates such as metal sulfides and oxides may be present in SN ejecta (Cherchneff & Dwek 2010). Larger dust masses arise from the assumption of a clumpy ejecta (Ercolano et al. 2007), but the final values always remain small between 200 and 600 days post-outburst. These results do not support the hypothesis that SNe are important dust contributors to galaxies locally and at high redshift. If SN explosions were to provide the large amounts of dust needed to reproduce the reddening of distant quasars and metal measurements in damped Ly $\alpha$  systems (Pei et al. 1991; Pettini et al. 1994; Bertoldi et al. 2003), the dust yield per SN needs to be as high as  $\sim 1 M_{\odot}$  (Dwek et al. 2007). Such a high value is difficult to reconcile with the small masses of warm dust detected in the IR.

The latest data on SN remnants (SNRs) obtained with the submillimeter (submm) *Herschel* Telescope have cast a new light on the dust released by SN events. A large mass of cold ejecta dust, amounting to  $0.08 M_{\odot}$ , has been derived in the 330 yr old SNR Cas A (Barlow et al. 2010; Sibthorpe et al. 2010). In the Crab Nebula, a 1050 yr old pulsar wind SNR, cool dust was recently detected in the filaments and the derived dust masses amount to  $0.1\text{--}0.24 M_{\odot}$ , depending on the type of dust assumed (Gomez et al. 2012). Finally,  $0.4\text{--}0.7 M_{\odot}$  of cool ejecta dust have been inferred from submm flux data in

the young remnant SN1987A (Matsuura et al. 2011). These cold dust masses are large compared with those derived from IR observations and imply that either dust grains continue to form in the SNR decades after their initial condensation at day  $\sim 400$  or the IR observations only probe the dust content of the ejecta at early times when the ejecta dust may still form at later epochs in the nebular phase. The first scenario is unlikely because high gas temperatures are required to overcome the activation energy barriers characterizing the neutral processes involved in the nucleation of dust, and large densities are also necessary to ensure the efficiency of these reactions (Cherchneff 2010). These two conditions are not met in the SNR gas.

In the present paper, we report on new physico-chemical models of the stratified ejecta of SNe with different progenitor masses and solar metallicity. We study the formation of molecules and small molecular clusters implicated in the nucleation phase of the synthesis of dust and describe the different steps involved in dust nucleation following a chemical kinetic approach, following previous studies of the chemistry of primeval SNe (Cherchneff & Lilly 2008; Cherchneff & Dwek 2009, 2010). We include the new nucleation chemistry of small silicate clusters as described by Goumans & Bromley (2012). These clusters set an upper limit on the final dust mass formed since they represent a bottleneck to the condensation phase of dust. In Section 2, we describe the physical and chemical model of stratified ejecta. The results on elements, molecules, and dust clusters are presented in Section 3, where we discuss the impact of the  $^{56}\text{Ni}$  mass and compare our results with existing studies. A discussion follows in Section 4.

## 2. THE PHYSICAL AND CHEMICAL MODEL

The helium core of a massive star exploding as an SN is crossed by a blast wave that deposits energy in the gas. When encountering the progenitor envelope, this wave triggers a reverse shock at the base of the envelope that propagates inward and produces Rayleigh–Taylor instabilities and macroscopic mixing in the helium core. The mixing ceases after a few days (Joggerst et al. 2010) and the partial fragmentation of the helium core proceeds with time. Radioactive  $^{56}\text{Ni}$  decays into  $^{56}\text{Co}$  on a timescale of a few days. In turn,  $^{56}\text{Co}$  decays into  $^{56}\text{Fe}$  with a half-life of  $\sim 113$  days, creating a flux of  $\gamma$  photons that pervades the ejecta. The degradation of  $\gamma$ -rays to X-rays and ultraviolet (UV) photons occurs by Compton scattering and creates a population of fast Compton electrons in the ejecta. These fast electrons ionize the gas and produce ions such as  $\text{Ar}^+$ ,  $\text{Ne}^+$ , and  $\text{He}^+$  that are key species in the ejecta chemistry. The physical models of the stratified ejecta are presented in the next section, followed by a section on the chemistry.

### 2.1. Physical Model

Stratified ejecta are considered for massive stellar progenitors of masses 12, 15, 19, and 25  $M_\odot$ . This choice of progenitor masses is based on the availability of SN nucleosynthesis models in the literature and corresponds to values derived from the estimate of  $^{56}\text{Ni}$  mass from the SN light curve. Most Type II-P SNe originate from the explosion of massive stars with typical masses of 12  $M_\odot$ –15  $M_\odot$ . In the cases of SN1987A and Cas A, a progenitor of mass  $\sim 19 M_\odot$  has been inferred (Woosley 1988; Krause et al. 2008). The most massive progenitor, 25  $M_\odot$ , is considered as a surrogate of the massive SNe characterizing the explosion of Population II stars at high redshift (Tumlinson

2006), whereas the 12  $M_\odot$  progenitor represents low-mass SNe, including some members of the faint SN subclass characterized by a low-mass progenitor (8–10  $M_\odot$ ) and a low mass of processed  $^{56}\text{Ni}$ . In these faint SNe, e.g., SN2011ht (Mauerhan et al. 2012), dust forms as early as  $\sim 100$  days after explosion.

The stratified ejecta is described by the mass zones of the progenitor core given by the explosion models and we assume that the gas within each zone is fully microscopically mixed. No gas leakage between different zones is assumed. The initial chemical composition of the ejecta in the form of the elemental mass yields are taken from Rauscher et al. (2002) for the 15, 19, and 25  $M_\odot$  progenitors, while that of the 12  $M_\odot$  progenitor is from Woosley & Heger (2007). The elemental mass yields for all progenitors are summarized in Table 1.

Synthetic ejecta temperature and number density profiles were constructed based on the explosion model for a Type II-P SN with a 17  $M_\odot$  progenitor provided by Nozawa et al. (2010). For the sake of simplicity, we choose this model for all SN progenitors studied and the gas parameters are listed in Table 2 for the 15  $M_\odot$  progenitor as a function of post-explosion time and ejecta zoning. The temperature variation as a function of post-explosion time is given by

$$T_{\text{gas}}(M_r, t) = T_{\text{gas}}(M_r, 100) \times (t/100)^{-1.26}, \quad (1)$$

where  $T_{\text{gas}}(M_r, 100)$  is the gas temperature 100 days after explosion,  $M_r$  is the mass coordinate, and  $t$  is time. In the explosion model of Nozawa et al. (2010), the gas temperature varies with the mass coordinate over the ejecta owing to differential deposition of energy in the helium core. We then assume different initial temperatures with mass zones at 100 days for all progenitor models; the initial  $T_{\text{gas}}(M_r, 100)$  values are given in Table 2.

Assuming homologous expansion, the gas density is given by

$$n_{\text{gas}}(M_r, t) = \rho_{\text{gas}}(M_r, 100)/\mu(M_r, t) \times (t/100)^{-3}, \quad (2)$$

where  $\rho_{\text{gas}}(M_r, 100)$  and  $\mu(M_r, t)$  are the gas density 100 days post-outburst and the gas mean molecular weight at time  $t$  in the mass zone of coordinate  $M_r$ , respectively. According to the gas density profiles in Figure 2 of Nozawa et al. (2010), we assume a constant initial gas density  $\rho_{\text{gas}}(100)$  independent of mass coordinate for all progenitor masses, with  $\rho_{\text{gas}}(100) = 1.1 \times 10^{-11} \text{ g cm}^{-3}$ . All progenitor masses are characterized by an explosion energy of  $1 \times 10^{51} \text{ erg}$ , while the effective  $\gamma$ -ray optical depths at 100 days  $\tau(100)$  have been estimated according to Cherchneff & Dwek (2009) and are 13.5, 17.5, 23, and 29 for the 12, 15, 19, and 20  $M_\odot$  progenitors, respectively.

### 2.2. Chemical Model

The various atoms, molecules, and ions assumed to form in the SN ejecta and considered in our chemical scheme are summarized in Table 3. We model the chemistry in the ejecta considering all possible types of chemical reactions relevant to hot and dense environments. All chemical pathways that lead to the formation of linear molecules, carbon chains and rings, and small dust clusters include neutral–neutral processes such as termolecular, bimolecular, and radiative association reactions and charge exchange reactions, whereas destruction is described by thermal fragmentation, neutral–neutral processes (i.e., oxidation reactions of carbon chains and all reverse processes of the formation reactions), ion–molecule recombination processes, and charge exchange reactions.

The nucleation scheme to silica and silicate clusters is illustrated in Figure 1 and the full chemical network describing

**Table 1**  
Initial (Post-explosive) Elemental Mass Yields (in  $M_{\odot}$ ) as a Function of Progenitor Mass and Ejecta Zone<sup>a</sup>

Zone	$\mu(\text{gas})$	C/O	He	C	O	Ne	Mg	Al	Si	S	Ar	Fe	Ni
12 $M_{\odot}$													
1A (1.7–1.76 $M_{\odot}$ )	32.02	0.215	0	9.76(−8)	6.71(−7)	3.05(−7)	7.32(−6)	1.16(−5)	2.50(−2)	2.38(−2)	3.29(−3)	4.76(−3)	3.54(−5)
1B (1.76–1.89 $M_{\odot}$ )	17.38	3.68(−4)	0	2.86(−5)	0.104	1.30(−5)	5.72(−3)	4.16(−4)	1.56(−2)	2.60(−3)	7.41(−5)	5.07(−5)	1.24(−4)
2 (1.89–2.03 $M_{\odot}$ )	17.3	7.87(−3)	0	5.46(−4)	9.24(−2)	3.50(−2)	8.68(−3)	5.60(−4)	6.02(−4)	4.20(−5)	1.19(−5)	1.29(−4)	0
3 (2.03–2.19 $M_{\odot}$ )	15.28	0.34	0	3.04(−2)	0.118	7.36(−3)	2.72(−3)	2.08(−4)	1.47(−4)	3.52(−5)	1.42(−5)	8.16(−5)	0
4 (2.19–2.35 $M_{\odot}$ )	4.91	15.39	0.117	3.68(−2)	3.20(−3)	2.08(−3)	8.00(−4)	9.28(−6)	1.47(−4)	4.96(−5)	1.31(−5)	1.76(−4)	0
5 (2.35–3.27 $M_{\odot}$ )	4.05	1.27	0.911	1.93(−4)	2.02(−4)	1.01(−2)	6.62(−4)	6.75(−5)	7.54(−4)	3.86(−4)	1.01(−4)	1.29(−3)	0
15 $M_{\odot}$													
1A (1.79–1.88 $M_{\odot}$ )	35.49	5.9(−2)	0	1.45(−7)	3.30(−6)	0	1.39(−5)	1.98(−5)	3.19(−2)	1.96(−2)	4.02(−3)	1.65(−2)	2.80(−4)
1B (1.88–1.98 $M_{\odot}$ )	20.89	2.1(−3)	0	6.91(−6)	4.36(−2)	1.05(−5)	3.92(−4)	4.97(−5)	3.12(−2)	1.25(−2)	7.38(−4)	1.25(−4)	1.24(−7)
2 (1.98–2.27 $M_{\odot}$ )	17.17	5.50(−3)	0	9.26(−4)	0.225	1.51(−2)	1.60(−2)	2.10(−3)	2.10(−2)	2.52(−3)	4.06(−5)	2.30(−5)	0
3 (2.27–2.62 $M_{\odot}$ )	17.12	1.60(−2)	0	2.77(−3)	0.234	7.76(−2)	1.75(−2)	1.92(−3)	1.76(−3)	6.84(−5)	1.72(−5)	3.38(−5)	0
4A (2.62–2.81 $M_{\odot}$ )	14.99	0.367	6.06(−6)	4.04(−2)	0.147	2.97(−3)	1.64(−4)	2.34(−4)	7.08(−5)	3.47(−5)	9.56(−6)	2.15(−5)	0
4B (2.81–3.04 $M_{\odot}$ )	10.66	0.735	3.08(−2)	6.16(−2)	0.112	1.40(−2)	7.11(−4)	1.91(−5)	1.05(−4)	4.39(−5)	8.64(−6)	4.01(−5)	0
5 (3.04–3.79 $M_{\odot}$ )	4.14	21.3	0.705	2.72(−2)	1.66(−3)	1.19(−3)	3.86(−4)	5.25(−5)	4.84(−4)	2.91(−4)	1.20(−5)	8.40(−4)	0
6 (3.79–4.14 $M_{\odot}$ ) <sup>b</sup>	4.05	1.18	0.341	9.13(−5)	9.58(−5)	5.48(−4)	1.79(−4)	2.43(−5)	2.27(−4)	1.37(−4)	5.34(−6)	4.06(−4)	0
19 $M_{\odot}$													
1A (1.77–1.88 $M_{\odot}$ )	35.35	0.156	1.39(−6)	8.10(−8)	6.89(−7)	0	1.69(−5)	2.46(−5)	3.77(−2)	2.26(−2)	4.52(−3)	2.47(−2)	3.25(−4)
1B (1.88–2.18 $M_{\odot}$ )	22.47	1.30(−3)	0	1.15(−4)	0.118	1.05(−4)	8.79(−4)	2.18(−4)	9.88(−2)	5.59(−2)	1.54(−2)	3.10(−3)	6.19(−6)
2 (2.18–3.86 $M_{\odot}$ )	16.89	6.54(−2)	0	5.92(−2)	1.16	0.34	8.41(−2)	9.12(−3)	1.51(−2)	1.28(−3)	1.21(−4)	7.54(−4)	0
3 (3.86–4.00 $M_{\odot}$ )	15.11	0.36	0	2.89(−2)	0.107	2.81(−3)	2.01(−3)	1.63(−5)	1.11(−4)	3.19(−5)	8.94(−6)	7.82(−5)	0
4 (4.00–4.49 $M_{\odot}$ )	10.32	0.64	7.68(−2)	0.126	0.263	1.32(−2)	5.44(−3)	5.30(−5)	3.75(−4)	1.40(−4)	3.47(−5)	3.76(−4)	0
5 (4.49–5.26 $M_{\odot}$ )	4.12	3.93	0.743	1.27(−2)	4.30(−3)	1.07(−2)	5.01(−4)	5.99(−5)	5.53(−4)	3.21(−4)	7.04(−5)	9.83(−4)	0
6 (5.26–5.62 $M_{\odot}$ ) <sup>b</sup>	4.06	1.8	0.352	1.26(−4)	9.24(−5)	5.69(−4)	2.27(−4)	3.19(−5)	2.55(−4)	1.50(−4)	3.32(−5)	4.55(−4)	0
25 $M_{\odot}$													
1A (2.1–2.33 $M_{\odot}$ )	34.26	...	2.91(−6)	0	0	0	4.91(−5)	4.80(−5)	8.92(−2)	5.15(−2)	9.93(−3)	3.20(−2)	5.43(−4)
1B (2.33–2.51 $M_{\odot}$ )	26.18	4.03(−4)	0	8.18(−6)	2.84(−2)	1.71(−5)	5.90(−5)	6.46(−5)	8.87(−2)	4.34(−2)	8.53(−3)	3.81(−4)	1.36(−6)
2 (2.51–2.98 $M_{\odot}$ )	19.34	4.18(−4)	0	8.70(−5)	0.278	6.07(−5)	7.22(−3)	6.95(−4)	0.116	3.74(−2)	9.17(−3)	1.32(−4)	0
3 (2.98–5.69 $M_{\odot}$ )	17.01	2.32(−2)	0	4.3(−2)	1.95	0.44	0.129	2.12(−2)	5.81(−2)	8.29(−3)	1.09(−3)	1.20(−4)	0
4A (5.69–6.22 $M_{\odot}$ )	15.04	0.33	0	0.102	0.406	5.03(−3)	3.02(−4)	7.15(−5)	1.76(−4)	8.94(−5)	3.16(−5)	3.95(−5)	0
4B (6.22–7.11 $M_{\odot}$ )	12.40	0.49	6.17(−2)	0.231	0.525	4.64(−2)	2.61(−3)	1.36(−4)	3.18(−4)	1.40(−4)	4.98(−5)	7.56(−5)	0
5 (7.11–8.07 $M_{\odot}$ )	4.05	35.9	0.919	1.30(−2)	4.82(−4)	1.50(−3)	4.78(−4)	7.21(−5)	6.08(−4)	3.62(−4)	8.61(−5)	1.00(−3)	0
6 (8.07–8.30 $M_{\odot}$ ) <sup>b</sup>	4.05	1.57	0.232	6.89(−5)	5.83(−5)	3.71(−4)	1.22(−4)	1.77(−5)	1.54(−4)	9.35(−5)	2.13(−5)	2.76(−4)	0

**Notes.** The zone extension (in mass coordinates  $M_{\odot}$ ), the mean molecular weight (in  $\text{g cm}^{-3}$ ), and the C/O ratio are also given for each zone.

<sup>a</sup> Data for the 12  $M_{\odot}$  progenitor are from Woosley & Heger (2007), while data for the 15, 19, and 25  $M_{\odot}$  progenitors are from Rauscher et al. (2002).

<sup>b</sup> Yields for atomic N in zone 6 are 8.37(−3), 3.34(−3), and 2.93(−3) for the 15, 19, and 25  $M_{\odot}$  progenitors, respectively.

**Table 2**  
Gas Temperature and Number Density Variation with Post-explosion Time for Each Zone of the SN Ejecta with a 15  $M_{\odot}$  Progenitor<sup>a</sup>

15 $M_{\odot}$	Zone 1A		Zone 1B		Zone 2		Zone 3		Zone 4A		Zone 4B		Zone 5		Zone 6	
Time (days)	$T$	$n_{\text{gas}}$	$T$	$n_{\text{gas}}$	$T$	$n_{\text{gas}}$	$T$	$n_{\text{gas}}$	$T$	$n_{\text{gas}}$	$T$	$n_{\text{gas}}$	$T$	$n_{\text{gas}}$	$T$	$n_{\text{gas}}$
100	12000	1.8(11)	11600	3.1(11)	10400	3.7(11)	8779	3.8(11)	7980	4.3(11)	7580	6.1(11)	6490	1.6(12)	6010	1.6(12)
300	3006	6.7(9)	2906	1.1(10)	2605	1.4(10)	2199	1.4(10)	1998	1.6(10)	1899	2.3(10)	1626	5.9(10)	1506	6.0(10)
600	1255	8.3(8)	1213	1.4(9)	1088	1.7(9)	918	1.8(9)	835	2.0(9)	793	2.8(9)	679	7.4(9)	629	7.5(9)
900	753	2.5(8)	728	4.3(8)	653	5.1(8)	551	5.2(8)	501	5.9(8)	476	8.4(8)	407	2.2(9)	377	2.2(9)
1200	524	1.0(8)	507	1.8(8)	454	2.1(8)	383	2.2(8)	349	2.5(8)	331	3.5(8)	283	9.3(8)	262	9.3(8)
1500	396	5.3(7)	382	9.2(7)	343	1.1(8)	289	1.1(8)	263	1.3(8)	250	1.8(8)	214	4.7(8)	198	4.8(8)

**Note.** <sup>a</sup> The temperature  $T$  is in Kelvin and the gas number density  $n_{\text{gas}}$  is in  $\text{cm}^{-3}$ .

the nucleation of silicate clusters is listed in Table 10 in the Appendix. Small silica clusters form according to the processes described by Cherchneff & Dwek (2010), where the study of SiO dimerization by Zachariah & Tsang (1993) was used. In the present study, we consider as “silica” the ensemble of  $(\text{SiO})_n$  clusters that form, as these small clusters will condense to form amorphous silica. A possible disproportionation into  $\text{SiO}_2$  and  $\text{Si}_2$  components in the condensed amorphous compound is to

be expected (Reber et al. 2008), but we ignore a separation of these two phases in the present study. The description of the growth pathways of small silicate clusters, namely, forsterite dimer  $(\text{Mg}_2\text{SiO}_4)_2$  and enstatite dimer  $(\text{MgSiO}_3)_2$ , is based on the work by Goumans & Bromley (2012). This study indicates possible chemical routes to the formation of the silicate dimers involving the formation of the SiO dimer  $(\text{SiO})_2$  ring and its growth to  $\text{Si}_2\text{O}_3$  through the reaction with  $\text{O}_2$  and SO. The

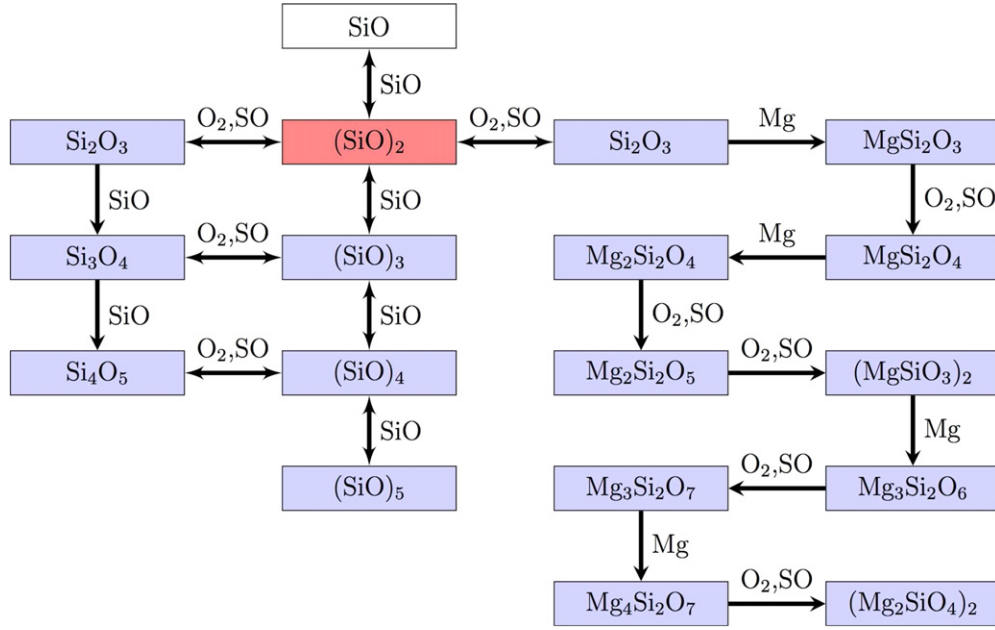


**Figure 1.** Chemical nucleation processes involved in the formation of enstatite and forsterite dimers ( $\text{Mg}_2\text{Si}_2\text{O}_6$  and  $\text{Mg}_4\text{Si}_2\text{O}_8$ , respectively), according to Goumans & Bromley (2012). Reactant species are given for each process.  
(A color version of this figure is available in the online journal.)

**Table 3**  
Chemical Species and Dust Clusters Included in the Chemical Model of the SN Ejecta

Elements									
O	Si	S	C	Mg	Al	Fe	He	Ne	Ar
Ions									
O <sup>+</sup>	Si <sup>+</sup>	S <sup>+</sup>	C <sup>+</sup>	Mg <sup>+</sup>	Al <sup>+</sup>	Fe <sup>+</sup>	He <sup>+</sup>	Ne <sup>+</sup>	Ar <sup>+</sup>
SiO <sup>+</sup>	CO <sup>+</sup>	O <sub>2</sub> <sup>+</sup>	SO <sup>+</sup>						
Molecules									
O <sub>2</sub>	CO	SiO	SO	NO	AlO	FeO	MgO	CO <sub>2</sub>	
CN	CS	SiS	SiC	FeS	MgS	S <sub>2</sub>	N <sub>2</sub>		
Clusters									
C <sub>2</sub>	C <sub>3</sub>	C <sub>4</sub>	C <sub>5</sub>	C <sub>6</sub>	C <sub>7</sub>	C <sub>8</sub>	C <sub>9</sub>	C <sub>10</sub>	
Si <sub>2</sub>	Si <sub>3</sub>	Si <sub>4</sub>	Mg <sub>2</sub>	Mg <sub>3</sub>	Mg <sub>4</sub>	Fe <sub>2</sub>	Fe <sub>3</sub>	Fe <sub>4</sub>	
Si <sub>2</sub> C <sub>2</sub>	Mg <sub>2</sub> S <sub>2</sub>	Mg <sub>3</sub> S <sub>3</sub>	Mg <sub>4</sub> S <sub>4</sub>	Fe <sub>2</sub> S <sub>2</sub>	Fe <sub>3</sub> S <sub>3</sub>	Fe <sub>4</sub> S <sub>4</sub>			
Si <sub>2</sub> O <sub>2</sub>	Si <sub>3</sub> O <sub>3</sub>	Si <sub>4</sub> O <sub>4</sub>	Si <sub>5</sub> O <sub>5</sub>	SiO <sub>2</sub>	Si <sub>2</sub> O <sub>3</sub>	Si <sub>3</sub> O <sub>4</sub>	Si <sub>4</sub> O <sub>5</sub>		
MgSi <sub>2</sub> O <sub>3</sub>	MgSi <sub>2</sub> O <sub>4</sub>	Mg <sub>2</sub> Si <sub>2</sub> O <sub>4</sub>	Mg <sub>2</sub> Si <sub>2</sub> O <sub>5</sub>	Mg <sub>2</sub> Si <sub>2</sub> O <sub>6</sub>	Mg <sub>3</sub> Si <sub>2</sub> O <sub>6</sub>	Mg <sub>3</sub> Si <sub>2</sub> O <sub>7</sub>	Mg <sub>4</sub> Si <sub>2</sub> O <sub>7</sub>	Mg <sub>4</sub> Si <sub>2</sub> O <sub>8</sub>	
Mg <sub>2</sub> O <sub>2</sub>	Mg <sub>3</sub> O <sub>3</sub>	Mg <sub>4</sub> O <sub>4</sub>	Fe <sub>2</sub> O <sub>2</sub>	Fe <sub>3</sub> O <sub>3</sub>	Fe <sub>4</sub> O <sub>4</sub>				

subsequent pathway involves the addition of a Mg atom into the  $\text{Si}_2\text{O}_3$  structure. The later growth of clusters is described by one oxygen-addition step followed by one Mg inclusion as a recurrent growth scenario. We consider different oxidizing agents, including atomic O,  $\text{O}_2$ , and SO, and find that reactions with  $\text{O}_2$  and SO are prevalent. Atomic oxygen is very abundant in the O-rich zones 1B and 2, but its inclusion in clusters proceeds through slow reactions such as termolecular (cluster + O + M  $\rightarrow$  [cluster + O] + M) and radiative association (cluster + O  $\rightarrow$  [cluster + O] +  $h\nu$ ) processes. Both processes have low reaction rates compared with the bimolecular reaction with  $\text{O}_2$  (typically  $10^{-31} \text{ cm}^6$  and  $10^{-17} \text{ cm}^3 \text{ s}^{-1}$ ) and the net formation rate is lower by a factor  $10^4$  and 10–100 for termolecular and radiative processes, respectively. According to Goumans & Bromley (2012), both oxygen and magnesium addition processes to grow silicate clusters are downhill and no activation barrier is considered for the rates.

Ionization of atoms in the ejecta occurs via collision with Compton electrons. The radioactive decay of  $^{56}\text{Ni}$  to  $^{56}\text{Co}$  and  $^{56}\text{Fe}$  creates  $\gamma$ -rays that degrade to X-rays and UV photons through collisions with thermal electrons, thus inducing the creation of a population of Compton electrons in the gas. These fast electrons ionize atoms and destroy chemical species in the ejecta. The time-dependent destruction rate by Compton electrons  $k_C$  for species  $i$  in  $\text{s}^{-1}$  is calculated using Equation (4) of Cherchneff & Dwek (2009). The rate is re-scaled according to the amount of  $^{56}\text{Ni}$  produced by the explosion of the various progenitors and, following Cherchneff & Dwek (2009), the rate values are converted to an Arrhenius temperature-dependent form whose parameters are listed in Table 11 in the Appendix. The interaction of the Compton electrons with molecules leads to their dissociation, ionization, and fragmentation into ionic products. The branching ratios for the different processes depend on  $W_i$ , the mean energy per ion pair for a given species. Available



values of  $W_i$  for molecules that form in the ejecta are listed in Table 11. When data are not available, we simply assume values similar to those for O for elements and CO for molecules. The impact on molecules and dust clusters of the UV radiation field resulting from the degradation of  $\gamma$ -rays was assessed by Cherchneff & Dwek (2009), who found that the destruction of molecules and dust precursors by this UV radiation field was not important compared with destruction by Compton electrons. We thus ignore UV radiation for the rest of the present study.

### 3. RESULTS

To better understand the chemical composition of several post-explosion ejecta reflecting the evolution and nucleosynthesis of massive stars, we model the formation of molecules and dust clusters in the ejecta of four SNe with progenitors of mass 12, 15, 19, and 25  $M_\odot$ . The mass of  $^{56}\text{Ni}$  is either 0.075 or 0.01  $M_\odot$ . The 15  $M_\odot$  progenitor with  $M(^{56}\text{Ni}) = 0.075 M_\odot$  is chosen as the “standard case,” for which results on molecules and dust are presented in Section 3.1. The impact of varying the  $^{56}\text{Ni}$  mass is studied in Section 3.2. More massive progenitors are considered in Section 3.3, while results for a low-mass progenitor with a small  $^{56}\text{Ni}$  mass are given in Section 3.4. Finally, results on elements are shown in Section 3.5 and various dust formation models in SN are compared in Section 3.6.

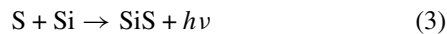
#### 3.1. 15 $M_\odot$ Progenitor

We present the masses of molecules, dust clusters, and elements as a function of time after explosion (in days) for the “standard case.” The chemistry is followed from day 100 until day 1500, a time span that covers the initial formation of molecules at early times until the dust cluster synthesis is fully completed some 4 yr after outburst.

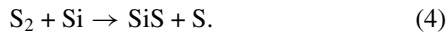
##### 3.1.1. Molecules

We find that the zones of the He core are efficient at forming large amounts of molecules, except for the outermost zone 6. Because the ejecta is assumed to be hydrogen-free, the number of chemical species formed is limited; this poor chemistry typical of SN ejecta is well exemplified by the detection of only two molecules, CO and SiO, in several SNe (Danziger et al. 1988; Roche et al. 1991; Kotak et al. 2005), and CO in SNRs (Rho et al. 2009, 2012).

The innermost layer, zone 1A, is rich in iron, silicon, and sulfur, where the iron results from the decay of  $^{56}\text{Ni}$  and  $^{56}\text{Co}$ . The oxygen content of the zone is very low and precludes the formation of O-bearing species, metal oxides, and silicates. Zone 1A quickly converts most of the atomic sulfur and half of the atomic silicon mass into silicon sulfide, SiS, as illustrated in Figure 2. The SiS mass rapidly increases after  $\sim 200$  days to reach  $4.3 \times 10^{-2} M_\odot$  1500 days post-explosion. The main formation processes for SiS are the radiative association reaction



and the reaction



The latter process is not well characterized; it has no measured reaction rate and was included based on a process involving the reaction of atomic C with disulfur, for which a rate has been estimated at 300 K. Owing to the isovalence of carbon and silicon, a similar rate was adopted for Reaction (4). We tested the importance of Reaction (4) in the formation of SiS by

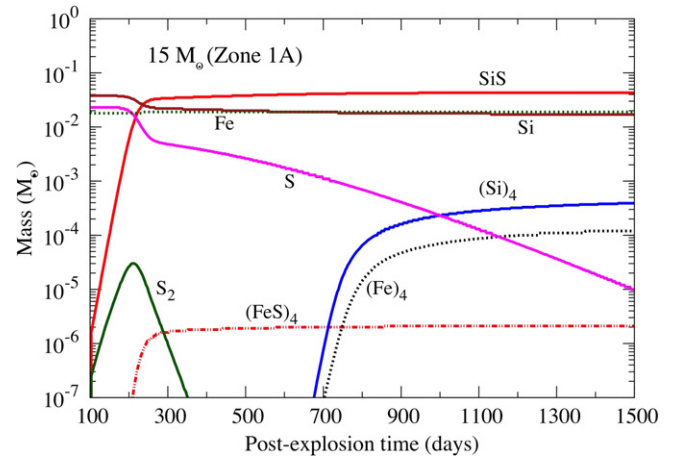


**Figure 2.** Molecules formed in the innermost zone, zone 1A, of the 15  $M_\odot$  ejecta. SiS is the prevalent species and depletes both Si and S atoms. Small masses of pure Fe clusters and iron sulfide (FeS) clusters also form.

(A color version of this figure is available in the online journal.)

removing it from the chemical network. SiS was then mainly formed by Reaction (3), with a similar efficiency and masses. Therefore, we conclude that the innermost zone of the He core overwhelmingly produces SiS due to the large S and Si content of the zone.

Carbon monoxide, CO, was the first molecule detected in SN1987A. The fundamental band at  $4.65 \mu\text{m}$  was observed between day 135 and day 260 (Danziger et al. 1988), while the CO first overtone transition at  $2.29 \mu\text{m}$  was detected at day 100 after the explosion (Spyromilio et al. 1988). CO was later detected in several other SNe (Cherchneff & Sarangi 2011). Once formed, CO can withstand harsh conditions in the ejecta because of its strong chemical bond. Depending on the C/O ratio characterizing each zone, CO formation limits the amount of leftover atomic oxygen or carbon in the gas phase and thus controls the chemistry of the gaseous and solid components of the gas. In the present case, most of the He core zones have C/O ratios less than one, except for the outer mass zone, zone 5 (see Table 1). The evolution of CO mass with post-explosion time for the He core zones is shown in Figure 3. CO masses derived from available observational data for SN1987A are also plotted for early times. In zones 4A, 4B, 2, and 3, CO forms as early as 200 days and reaches masses ranging from  $10^{-4}$  to  $10^{-2} M_\odot$ . The prevalent formation processes between 100 and 200 days are



and



The formation of  $\text{C}_2$  chains via radiative association reactions starts early on but, owing to the large atomic oxygen content,  $\text{C}_2$  is quickly converted to CO following Reaction (5). The formation of CO via oxidation of carbon chains prevails at early times, while Reaction (6) contributes to the growth of CO mass after day 300. The final CO mass summed over all zones at day 1500 is  $\sim 2 \times 10^{-1} M_\odot$ , much larger than the masses derived from IR data before day 600 in SN1987A (Liu & Dalgarno 1995). These large amounts of CO primarily form in zones 4A and 4B and do not trace efficient carbon dust formation in these two zones. These zones indeed form little or no carbon dust because carbon chains are quickly destroyed by oxidation reactions similar to Reaction (5) to form CO, thus impeding their growth into larger carbon clusters.

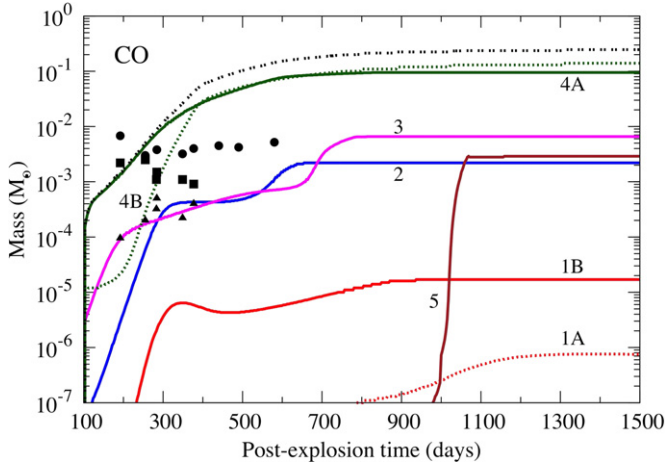


**Figure 3.** Evolution of CO masses with post-explosion time for the  $15 M_{\odot}$  progenitor as a function of ejecta zones (see Table 1 for zone labeling). The dotted gray line represents the mass summed over all zones. CO is prevalently produced by zones 4A and 4B, followed by zones 2 and 3. The CO mass reaches large values ( $\sim 10^{-1} M_{\odot}$ ) some 4 yr after explosion. CO masses derived from observations for SN1987A are also shown as symbols: local thermodynamic equilibrium (LTE; triangles) and non-LTE (squares) assumptions (Liu et al. 1992) and a thermal (circles) assumption (Liu & Dalgarno 1995).

(A color version of this figure is available in the online journal.)

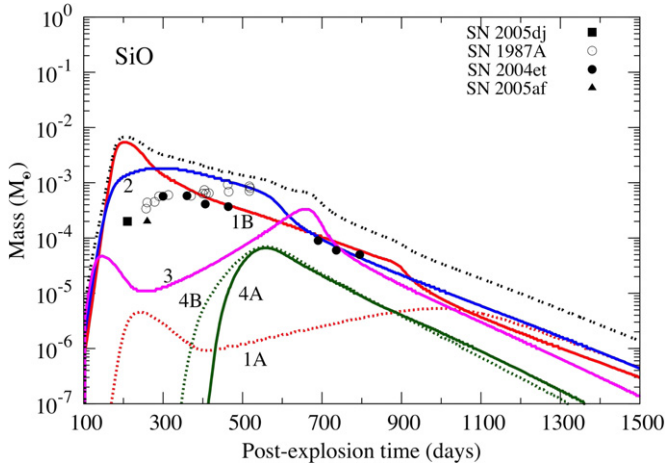


**Figure 4.** Evolution of SiO masses with post-explosion time for the  $15 M_{\odot}$  progenitor as a function of ejecta zones (see Table 1 for zone labeling). The dotted gray line represents the mass summed over all zones. SiO formation prevails at early times in zones 1B and 2 when zone 3 also contributes at later epochs. The SiO mass shows a strong decrease that reflects the formation of silica and silicate clusters in the ejecta O-rich zones. The masses derived from the observations of several SNe are also shown as symbols.

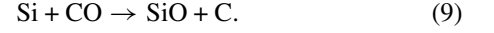
(A color version of this figure is available in the online journal.)

The oxygen-rich component of the He core includes zones 1B, 2, 3, 4A, and 4B, extending from  $1.88 M_{\odot}$  to  $3.04 M_{\odot}$  (see Table 1). Oxygen-bearing molecules are expected to form there but the zones are rich in inert gas, namely Ar (zone 1B) and Ne (zones 2 and 3). Ar and Ne atoms are ionized by Compton electrons and the ions ( $\text{Ar}^+$  and  $\text{Ne}^+$ ) are destroyed by both the recombination to their inert parents and the shrinkage in Compton electrons with time owing to the decreasing mass of  $^{56}\text{Ni}$ .  $\text{Ar}^+$  and  $\text{Ne}^+$  are detrimental to the formation and survival of molecules in these zones as they quickly destroy molecules. The mass of silicon oxide, SiO, formed in the various zones as a function of post-explosion time is shown in Figure 4. Superimposed are the SiO masses derived from IR observational data for several SNe. The mass follows a rapid increase at day

200 in zones 1B, 2, and 3, while the formation of SiO is delayed to 400 days in zones 4A and 4B. The prevalent formation process for SiO in zones 1B, 2, and 3 are the reactions



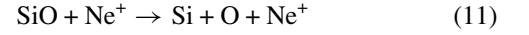
and



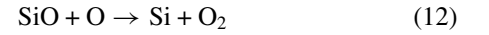
The prevalent destruction processes are



for zone 1B,



for zones 2 and 3, and

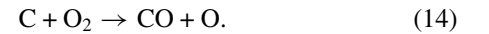


for both zones. Upon formation, SiO is destroyed by  $\text{Ar}^+$  and  $\text{Ne}^+$  following Reactions (10) and (11). The SiO mass for all zones shows a gradual and strong decrease, going from  $\sim 10^{-2} M_{\odot}$  at 200 days to  $\sim 10^{-6} M_{\odot}$  at 1500 days. Such a decline is also shown by the SiO masses derived from observations, for example, in SN2004et (Kotak et al. 2009). In this object, the SiO transition was detected at various periods and showed a gradual fading with time that is coupled to the evidence for dust synthesis in the ejecta. The destruction of SiO before 400 days results from thermal fragmentation and the destruction by  $\text{Ar}^+$  and  $\text{Ne}^+$  ions. At later times, SiO is depleted into silica and silicate clusters, as we will see in the next section, and acts as a direct dust synthesis tracer in the ejecta.

Apart from SiO, the formation of dioxygen,  $\text{O}_2$ , and sulfur monoxide, SO, prevails in the O-rich zones of the ejecta, as illustrated in Figure 5. Most of the  $\text{O}_2$  and SO molecules form in both zones 2, 3, and 4A. Their mass variation shows a similar trend with time, ranging from negligible masses before day 600 and reaching high-mass values after day 600. Dioxygen efficiently forms at early times from the radiative association reaction



but is quickly depleted in the formation of SiO and, to a minor extent, CO, following Reaction (8) and the reaction



At later times, the formation of AlO also contributes to the destruction of  $\text{O}_2$  via the reaction



while the reverse of Reaction (15) contributes to the reformation of  $\text{O}_2$ . The gradual depletion of SiO in silicate clusters allows the  $\text{O}_2$  mass to grow after day 600 to reach the large value of  $\sim 4 \times 10^{-1}$  at day 1500. The SO mass follows a trend similar to that of  $\text{O}_2$  because the SO formation is directly coupled to the formation of  $\text{O}_2$  by the reaction



and the SO destruction follows the reverse of Reaction (16). The final SO mass is large and amounts to  $2 \times 10^{-2} M_{\odot}$  at day 1500.

**Table 4**Masses of Molecules and Upper Limits on Dust Masses (Both in  $M_\odot$ ) at 1500 Days for the 15  $M_\odot$  Model with Two Values of  $^{56}\text{Ni}$  Mass ( $0.075 M_\odot$  and  $0.01 M_\odot$ )

Ejected Zones	Zone 1A	Zone 1B	Zone 2	Zone 3	Zone 4A	Zone 4B	Zone 5	Zone 6	Total
Zone mass ( $M_\odot$ )	9.6(−2)	9.5(−2)	0.292	0.347	0.195	0.225	0.75	0.347	2.35
Major elements	Si/S/Fe	Si/O	O/Mg/Si	O/Ne/Mg	O/C	He/O/C	He/C	He/N	
Molecules ( $M(^{56}\text{Ni}) = 0.075 M_\odot$ )									
SiO	4.4(−7)	3.0(−7)	4.4(−7)	1.3(−7)	3.1(−8)	2.0(−8)	...	...	1.4(−6)
O <sub>2</sub>	...	2.8(−5)	0.15	0.16	6.2(−2)	4.9(−3)	...	...	0.38
CO	7.5(−7)	1.7(−5)	2.2(−3)	6.6(−3)	9.5(−2)	0.14	2.9(−3)	...	0.25
SO	...	1.5(−2)	3.8(−3)	1.0(−4)	1.1(−4)	...	...	...	1.9(−2)
SiS	4.3(−2)	2.1(−7)	...	...	...	...	...	...	4.3(−2)
Total mass ( $M_\odot$ )	4.3(−2)	1.5(−2)	0.156	0.167	0.157	0.145	2.9(−3)	0	0.69
Efficiency	44.8%	15.8%	53.4%	48.1%	80.5%	64.7%	0.4%	0%	29.4%
Dust ( $M(^{56}\text{Ni}) = 0.075 M_\odot$ )									
Forsterite	...	5.3(−4)	4.4(−3)	5.9(−4)	2.7(−5)	2.5(−5)	...	...	5.6(−3)
Silica	...	6.0(−5)	5.1(−5)	...	...	...	...	...	1.1(−4)
Alumina	...	1.2(−5)	4.0(−3)	3.7(−3)	4.5(−5)	3.5(−5)	...	...	7.8(−3)
Pure iron	1.2(−4)	...	...	...	...	...	...	...	1.2(−4)
Iron sulfide	2.1(−6)	...	...	...	...	...	...	...	2.1(−6)
Pure silicon	3.9(−4)	...	...	...	...	...	...	...	3.9(−4)
Pure magnesium	...	...	2.2(−4)	2.5(−4)	...	...	...	...	4.7(−4)
Carbon	...	...	...	...	...	...	2.3(−2)	...	2.3(−2)
Silicon carbide	...	...	...	...	...	...	6.1(−4)	...	6.1(−4)
Total mass ( $M_\odot$ )	5.1(−4)	6.0(−4)	8.7(−3)	4.5(−3)	7.2(−5)	6.0(−5)	2.4(−2)	0	0.038
Efficiency(%)	0.53%	0.63%	3.0%	1.3%	3.7(−2)%	2.7(−2)%	3.2%	0%	1.62%
Molecules ( $M(^{56}\text{Ni}) = 0.01 M_\odot$ )									
SiO	3.8(−7)	2.1(−7)	4.3(−7)	1.3(−7)	3.1(−8)	2.0(−8)	...	...	1.2(−6)
O <sub>2</sub>	...	3.4(−4)	0.16	0.18	6.8(−2)	8.3(−3)	...	...	0.42
CO	7.6(−7)	1.7(−5)	2.2(−3)	6.6(−3)	9.5(−2)	0.14	2.8(−3)	...	0.25
SO	...	1.9(−2)	3.9(−3)	1.0(−4)	8.0(−5)	...	...	...	2.3(−2)
SiS	4.3(−2)	4.0(−7)	...	...	...	...	...	...	4.3(−2)
Total mass ( $M_\odot$ )	4.3(−2)	1.9(−2)	0.166	0.187	0.163	0.15	2.8(−3)	0	0.73
Efficiency	44.8%	20.0%	56.8%	53.9%	83.6%	66.7%	0.4%	0%	31.1%
Dust ( $M(^{56}\text{Ni}) = 0.01 M_\odot$ )									
Forsterite	...	6.7(−4)	2.3(−2)	1.8(−3)	1.2(−4)	7.2(−5)	...	...	2.6(−2)
Silica	...	6.0(−5)	4.1(−5)	...	...	...	...	...	1.1(−4)
Alumina	...	6.4(−5)	4.0(−3)	3.7(−3)	4.5(−5)	3.5(−5)	...	...	7.9(−3)
Pure iron	1.2(−4)	...	...	...	...	...	...	...	1.2(−4)
Iron sulfide	3.1(−6)	...	...	...	...	...	...	...	3.1(−6)
Pure silicon	3.8(−4)	...	...	...	...	...	...	...	3.8(−4)
Pure magnesium	...	...	6.8(−5)	3.4(−4)	...	...	...	...	4.1(−4)
Carbon	...	...	...	...	...	...	2.4(−2)	...	2.4(−2)
Silicon carbide	...	...	...	...	...	...	5.0(−4)	...	5.0(−4)
Total mass ( $M_\odot$ )	5.0(−4)	7.9(−4)	2.7(−2)	5.8(−3)	1.7(−4)	1.1(−4)	2.4(−2)	0	0.059
Efficiency	0.52%	0.83%	9.2%	1.7%	8.7(−2)%	4.9(−2)%	3.2%	0%	2.5%

**Note.** Efficiencies are the molecule or dust-to-gas mass ratio in each zone and for the total ejected zones of the He core.

We see that all chemistries responsible for the production of molecules are entangled and the final molecular component of the He core includes five molecules, namely, CO, O<sub>2</sub>, SiS, SO, and SiO. Aluminum oxide, AlO, is not included in the molecular component because it will quickly be depleted in (AlO)<sub>2</sub> and alumina dust clusters (see Section 3.1.2). We consider AlO as a “dust cluster” rather than a gas-phase molecule. The first four molecules form in the ejecta, participate in the ejecta chemistry prior to day 1500, and are ejected with large masses to later stages of the SN evolution, e.g., in the SNR phase. The SiO molecule, on the other hand, forms efficiently but is quickly depleted into the production of dust clusters after day 300 and, as such, enters the SNR phase with a much smaller mass than

the other species. The total mass of the molecular component of the SN ejecta is high and summarized as a function of zoning in Table 4. The final ejecta mass fraction residing in molecules at day 1500 amounts to  $\sim 30\%$  of the ejected mass for the 15  $M_\odot$  progenitor.

### 3.1.2. Dust

As discussed in Section 2.2, the description of the dust synthesis is based on the formation of large molecular clusters entering the nucleation phase of the dust grains. The nucleation phase involves the chemical kinetic description of the formation of these clusters from the gas phase. For silicates, our larger clusters are dimers of forsterite (Mg<sub>4</sub>Si<sub>2</sub>O<sub>8</sub>), while for carbon

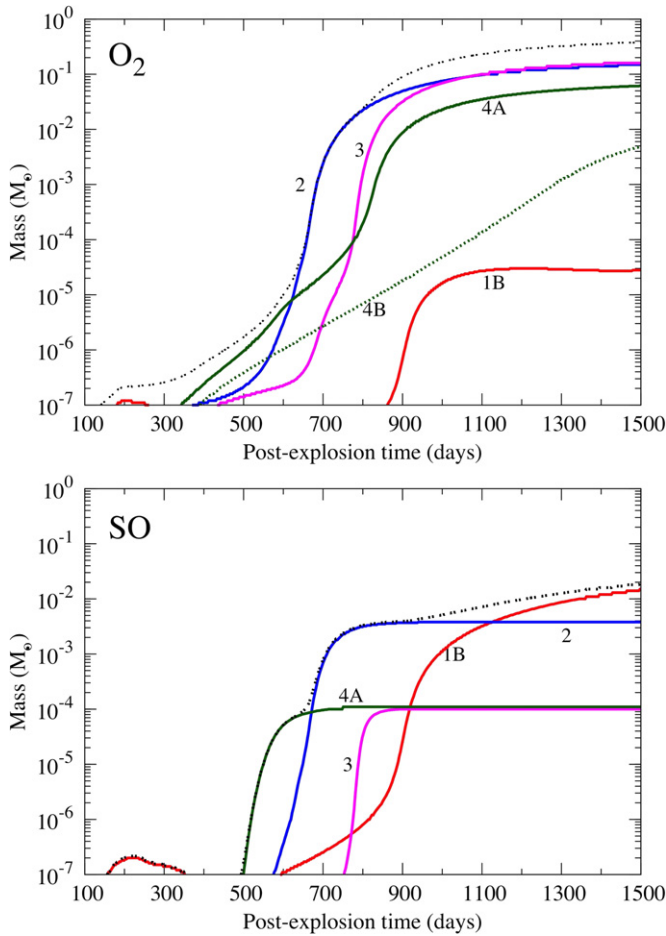


**Figure 5.** Evolution of masses of O-bearing species with post-explosion time for the  $15 M_{\odot}$  progenitor as a function of ejecta zones (see Table 1 for zone labeling), top: mass of  $O_2$ ; bottom: mass of  $SO$ . The dotted gray line represents the mass summed over all zones.

(A color version of this figure is available in the online journal.)

dust (possibly solid  $C_{60}$ ), we model the formation of the first carbon ring  $C_{10}$ . As for alumina, we are currently working on a chemical scheme to model alumina cluster formation based on cluster structures and the calculation of chemical rates but it is too premature to include such a scheme in our model. The most stable structure of  $Al_2O_3$  is kite-shaped (Archibong & St.-Amant 1999) and the formation of molecular  $Al_2O_3$  probably involves the dimerization of  $AlO$  and the possible addition of one oxygen atom via a bimolecular reaction with an O-bearing species. We can then safely assume that  $AlO$  molecules are precursors to alumina via the formation of  $(AlO)_2$  and that the  $AlO$  mass indicates an upper limit on the  $Al_2O_3$  mass that can form in the ejecta. The condensation phase involves the coalescence and coagulation of these clusters with each other, combined with surface growth if gas-phase growing agents are available. The condensation phase is not considered in the present study and the calculated masses of clusters thus represent an upper limit on the total mass of dust.

The modeled masses of dust clusters over all zones are illustrated in Figure 6 for the standard case. As discussed above, the condensation phase is not modeled and the cluster mass curves then flatten to their upper limit values once nucleation has taken place. As seen in Figure 6, there exist various events of cluster formation in the ejecta according to the chemical type of the dust and the zones in which the clusters form. The  $FeS$

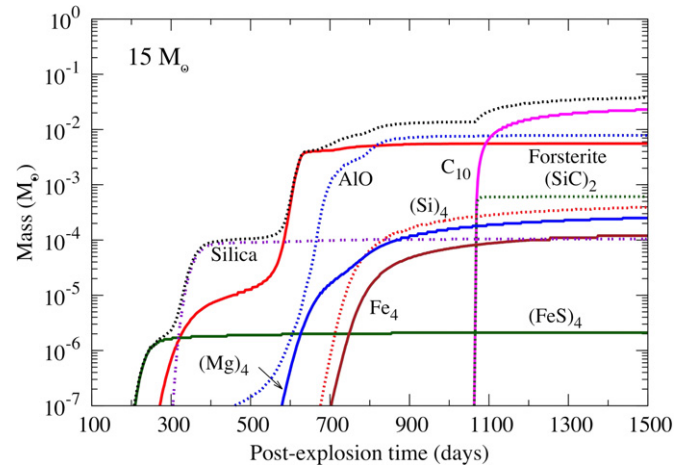


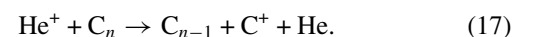
**Figure 6.** Evolution of dust cluster masses with post-explosion time for the  $15 M_{\odot}$  progenitor. For each cluster type, the masses have been summed over all ejecta zones. The dotted gray line represents the total cluster mass and provides an upper limit on the mass of dust that forms in the ejecta.

(A color version of this figure is available in the online journal.)

clusters are the first to form at day 250 in the innermost zone, zone 1A, followed by silica and forsterite clusters in zones 1B and 2 at day 350. Aluminum monoxide,  $AlO$ , forms after day 600 in zones 2 and 3. Most pure metal clusters form after day 700 and include  $Mg$  and  $Si$  in zones 2 and 3 and iron in zone 1A. Finally, carbon and silicon carbide clusters are synthesized in the outermost zone, zone 5, at late times ( $\sim 1050$  days).

The timing of dust production highly depends on the local chemistry characterizing the zones, as exemplified by the formation of silicates and carbon clusters. The forsterite dimer mass curve obtained for the various zones of the ejecta is shown in Figure 7. Forsterite first nucleates as early as 300 days in zone 1B and gradually grows to reach its maximum value at  $\sim 900$  days in this zone. These two nucleation phases are seen as two depletion events in the  $SiO$  mass curve for zone 1B (see Figure 4) and correspond to the formation of the  $O_2$  molecule at 300 days and 900 days in zone 1B (see Figure 5). The subsequent oxygen addition to silicate intermediates grows forsterite dimers. In zone 2, forsterite forms at  $\sim 600$  days from the depletion of  $SiO$  (see the drop in Figure 4 for zone 2) and the net formation of  $O_2$  molecules that permits the final growth to forsterite dimers. The formation of forsterite dimers is less effective in the other three zones of the ejecta and occurs at late epochs. Therefore, the gradual growth of the forsterite total mass, as shown in Figure 6, results from the chemistry of  $SiO$  formation and the growth of silicate clusters following the two-step mechanism of oxygen and magnesium addition proposed by Goumans & Bromley (2012).

The scenario for the growth of carbon small clusters is quite different. First of all, our results highlight the fact that carbon chains grow in significant amounts in the only carbon-rich zone of the ejecta, zone 5. Where oxygen overcomes carbon, e.g., in zone 4A and 4B, any carbon chain is destroyed by reaction with atomic O to form CO. Zone 5 is helium-rich and He atoms are ionized by Compton electrons. The produced ions are destroyed by recombination to He and by the decrease of Compton electrons with time.  $He^+$  is detrimental to the formation and survival of molecules in zone 5 (Lepp et al. 1990; Cherchneff & Dwek 2009, 2010) as the ion quickly destroys molecules following reactions such as





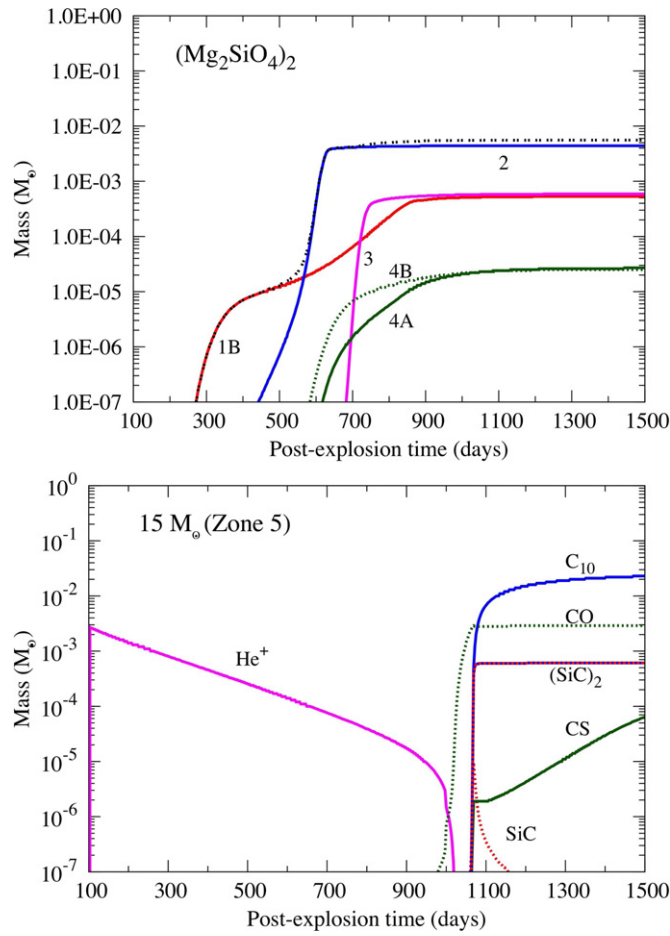
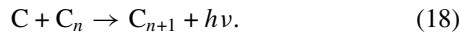


**Figure 7.** Top: forsterite dimer masses as a function of post-explosion time for the  $15 M_{\odot}$  progenitor and the various ejecta zones (see Table 1 for zone labeling). Bottom: the carbon-rich cluster masses with post-explosion time in zone 5 of the  $15 M_{\odot}$  progenitor. Clusters form once the  $\text{He}^+$  masses decrease to negligible values after day 1000.

(A color version of this figure is available in the online journal.)

Once the  $\text{He}^+$  ion mass becomes negligible after day 1000, molecules like CO, SiC,  $\text{C}_2$ , and CS quickly form. The growth of carbon chains is then efficient via radiative association reactions of the type



As the zone is C-rich, the low oxygen content hampers the destruction of carbon chains via reactions such as Reaction (14), which grow until the closure of the first ring,  $\text{C}_{10}$ . The formation of carbon clusters therefore strongly depends on the  $\text{He}^+$  content of the outer zone and the time at which the  $\text{He}^+$  abundance significantly decreases. Because of the very large initial He mass, the vanishing of  $\text{He}^+$  in the zone is delayed to  $\sim$ day 1050, resulting in a late formation of carbon and silicon carbide clusters. This late synthesis contributes to the time sequence of dust cluster production observed in Figure 6.

The gradual increase with time in cluster masses results in upper limits on dust mass ranging from  $10^{-5} M_{\odot}$  at  $\sim$ 300 days to  $\sim 4 \times 10^{-2} M_{\odot}$  more than 4 yr after explosion. This range of dust masses perfectly agrees with the values derived from observational data. At early times ( $200 < t < 600$  days), the masses derived from IR observations in several Type II-P SNe are small with typical values between  $10^{-5} M_{\odot}$  and  $10^{-3} M_{\odot}$ . These values correspond to our modeled cluster masses shown in Figure 6 for this time span. However, much

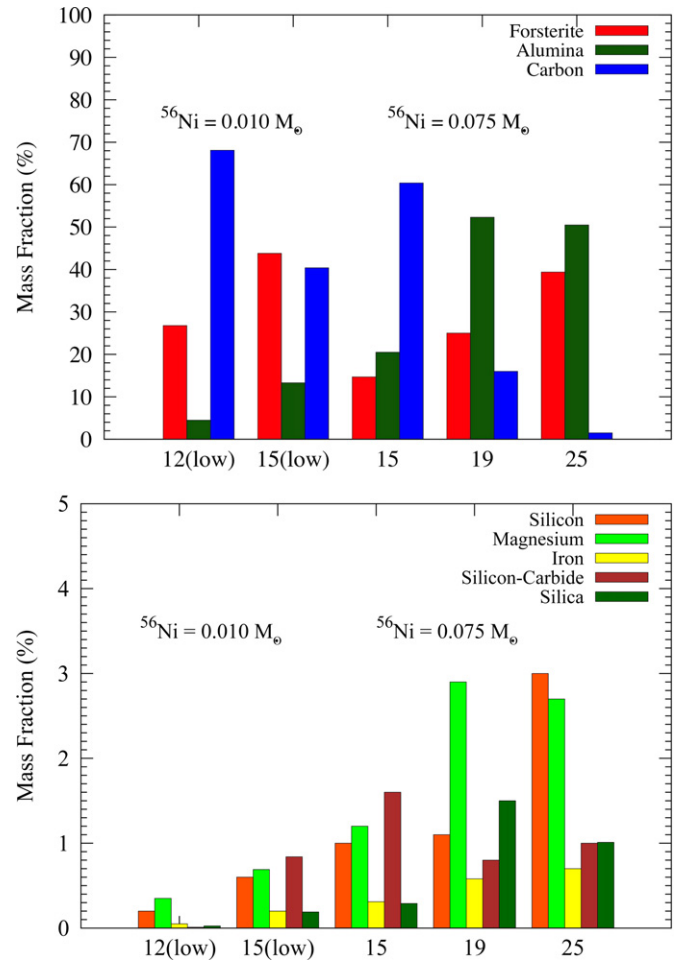


**Figure 8.** Top: the mass fraction (in %) of the major dust constituents entering the total dust mass produced at day 1500 vs. progenitor mass. Bottom: the mass fraction (in %) of the minor dust constituents entering the total dust mass produced vs. progenitor mass (in  $M_{\odot}$ ). The total dust mass produced is  $0.048 M_{\odot}$  and  $0.058 M_{\odot}$  for, respectively, the  $12 M_{\odot}$  and  $15 M_{\odot}$  progenitors with low  $^{56}\text{Ni}$  mass. For the 15, 19, and  $25 M_{\odot}$  progenitors with large  $^{56}\text{Ni}$  mass, the total dust mass produced is  $0.038$ ,  $0.035$ , and  $0.09 M_{\odot}$ , respectively.

(A color version of this figure is available in the online journal.)

larger dust masses are derived in SNRs from submm data. In Cas A,  $\sim 0.08 M_{\odot}$  of dust is inferred from the *Herschel* data (Barlow et al. 2010). In SN1987A, between  $0.4$  and  $0.7 M_{\odot}$  of dust is inferred to reproduce the *Herschel* fluxes (Matsuura et al. 2011), while  $0.1$ – $0.2 M_{\odot}$  of dust is found in the filamentary structures of the Crab Nebula by Gomez et al. (2012) with *Herschel*. These masses obviously result from fitting the spectral energy distribution of the objects at IR and submm wavelengths, implying that an initial dust composition is assumed. In the case of Cas A and the Crab Nebula, two types of dust are considered separately, namely, amorphous carbon (AC) and silicates, while for SN1987A, large iron spheres are also included to obtain a satisfactory fit of the flux data. Notwithstanding the presence of cool dust in SNRs in amounts larger than what is observed at early times in SN ejecta at IR wavelengths, the derived dust masses and chemical compositions are somewhat uncertain and strongly depend on the physical and chemical parameters used in SN ejecta and SNRs (e.g., the dust chemical composition, grain size distribution, and temperatures). The chemical composition of the dust is illustrated for all progenitor masses in Figure 8, where we assume that all clusters are spontaneously depleted in dust grains with 100% efficiency at all times. For our standard

**Table 5**  
 $^{56}\text{Ni}$  Mass (in  $M_\odot$ ) and Low and High Limits on Progenitor Mass (in  $M_\odot$ ) for a Sample of Type II-P SNe

Name	$^{56}\text{Ni}$ Mass	Low Limit	High Limit	Reference
SN1999em	0.02	12	14	Elmhamdi et al. (2003b)
SN2003gd	0.016	8	12	Smartt et al. (2004); Hendry et al. (2005)
SN2004dj	0.095	12	20	Wang et al. (2005); Vinkó et al. (2009)
SN2004et	0.068	23	25	Kotak et al. (2009)
SN2005af	0.027	13	15	Kotak et al. (2006)
SN2005cs	0.003	10	15	Pastorello et al. (2009)
SN2007od	0.02	10	11	Andrews et al. (2011); Inserra et al. (2011b)
SN2009bw	0.022	11	15	Inserra et al. (2011a)
SN2009js	0.007	6	16	Gandhi et al. (2013)
SN2011ht <sup>a</sup>	0.01	8	10	Mauerhan et al. (2012)
SN remnants				
SN1987A	0.075	14	20	Woosley (1988), Smartt (2009)
Cas A	...	18	20	Krause et al. (2008)
The Crab Nebula	...	8	12	Davidson & Fesen (1985); MacAlpine & Satterfield (2008)

**Notes.** The progenitor masses of well-studied SN remnants with Type II SN progenitors are also indicated.

<sup>a</sup> A high-mass progenitor ( $\geq 25 M_\odot$ ) with substantial ejecta fallback is also possible for this object.

case, the final dust composition and mass fraction at day 1500 consist of 60% AC, 20% alumina, 15% forsterite, and a few % pure metal clusters, namely, Si, Mg, Fe, silica, and silicon carbide clusters. This dust composition is different from that assumed in the analysis of IR and submm data and reflects the chemically controlled nucleation of dust clusters. The formation sequence and the gradual growth of dust clusters with time in the ejecta is a consequence of the ejecta chemistry that produces molecules combined with the nucleation processes of the various clusters. Hence, this gradual growth of clusters represents a genuine explanation for the existing discrepancy between the small dust masses found in SNe and the larger dust masses inferred in SNRs.

### 3.2. Impact of the $^{56}\text{Ni}$ Mass

The  $^{56}\text{Ni}$  mass produced by SNe can be derived from the variation of the optical light curves and  $H\alpha$  luminosities in the nebula phase (Elmhamdi et al. 2003a). From direct identification or by comparison with explosion models, a mass for the supergiant progenitors can be inferred. Table 5 lists some Type II-P SNe with estimated  $^{56}\text{Ni}$  masses and progenitor mass ranges. Most of the SNe have progenitor masses between 10 and  $15 M_\odot$  and typical  $^{56}\text{Ni}$  masses of  $0.01\text{--}0.02 M_\odot$ , except for SN1987A and SN1999em, which have much larger values for both progenitor and  $^{56}\text{Ni}$  masses. This dichotomy reflects the trends derived by Hamuy (2003) that more massive SNe produce more energetic explosions and SNe with greater energies produce larger  $^{56}\text{Ni}$  masses. To account for the low  $^{56}\text{Ni}$  mass SNe, we study the impact of the  $^{56}\text{Ni}$  mass on the ejecta chemistry of our standard  $15 M_\odot$  progenitor, while the results for a low-mass progenitor ( $12 M_\odot$ ) with a low  $^{56}\text{Ni}$  content ( $0.01 M_\odot$ ) are presented in Section 3.3.

The primary impact of a smaller  $^{56}\text{Ni}$  mass in the ejecta is to reduce the number of Compton electrons resulting from the degradation of a smaller amount of  $\gamma$ -rays. Therefore, fewer ions such as  $\text{Ar}^+$ ,  $\text{Ne}^+$ , and  $\text{He}^+$  are produced, enhancing the survival of molecules and clusters. The mass evolution of forsterite clusters and carbon rings versus post-explosion time are illustrated in Figure 9 for the two  $^{56}\text{Ni}$  mass values,  $0.01 M_\odot$  and  $0.075 M_\odot$ . The destruction of molecules from which clusters form (e.g.,  $\text{SiO}$  and  $\text{C}_2$ ) is not as severe for the low  $^{56}\text{Ni}$

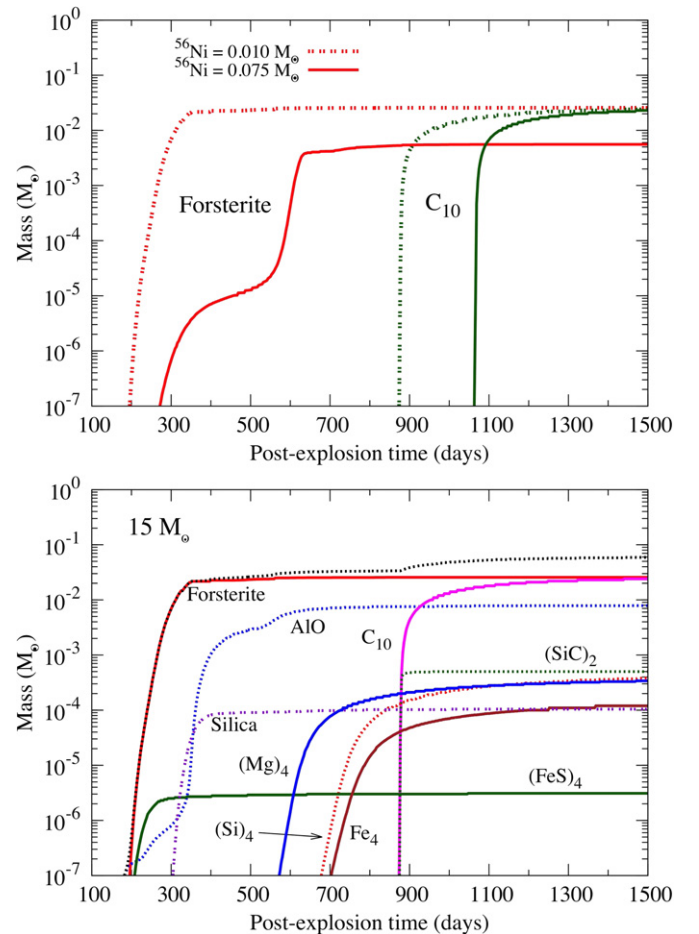


**Figure 9.** Top: mass of forsterite clusters and carbon rings for the  $15 M_\odot$  progenitor as a function of post-explosion time and  $^{56}\text{Ni}$  mass. Bottom: dust mass for the  $15 M_\odot$  progenitor as a function of post-explosion time for a  $^{56}\text{Ni}$  mass of  $0.01 M_\odot$ . The dotted gray line represents the total cluster mass. Dust clusters form at early time compared with the standard  $15 M_\odot$  case in Figure 6. (A color version of this figure is available in the online journal.)

mass case as it is for the standard case, because of the lower  $\text{Ne}^+$  and  $\text{He}^+$  ejecta content. Therefore, the formation of all clusters proceeds at early times and at large gas densities, resulting

**Table 6**  
Masses of Molecules and Upper Limits on Dust Masses (Both in  $M_{\odot}$ ) at 1500 Days for the  $19 M_{\odot}$  Progenitor with a  $^{56}\text{Ni}$  Mass of  $0.075 M_{\odot}$

Ejected Zones	Zone 1A	Zone 1B	Zone 2	Zone 3	Zone 4	Zone 5	Zone 6	Total
Zone mass ( $M_{\odot}$ )	0.11	0.302	1.68	0.141	0.486	0.774	0.358	3.85
Major elements	Si/S/Fe	Si/O	O/Ne/Mg	O/C	He/O/C	He/C	He/N	
Molecules								
SiO	3.9(−7)	2.0(−7)	1.9(−6)	7.9(−9)	7.2(−9)	...	...	2.5(−6)
O <sub>2</sub>	...	1.0(−5)	0.69	4.7(−2)	3.4(−2)	...	...	0.77
CO	1.5(−8)	2.7(−4)	0.13	6.7(−2)	0.29	7.2(−3)	...	0.50
SO	...	2.3(−2)	1.9(−3)	1.4(−4)	1.0(−7)	...	...	2.5(−2)
SiS	4.4(−2)	8.6(−5)	...	...	...	...	...	4.4(−2)
Total mass ( $M_{\odot}$ )	4.4(−2)	2.3(−2)	0.82	0.115	0.29	7.2(−3)	0	1.33
Efficiency	40.0%	7.6%	48.8%	81.6%	59.7%	0.93%	0%	33.9%
Dust								
Forsterite	...	1.7(−3)	6.5(−3)	1.6(−4)	2.5(−4)	...	...	8.6(−3)
Silica	...	3.0(−4)	2.3(−4)	...	...	...	...	5.3(−4)
Alumina	...	8.5(−6)	1.79(−2)	3.1(−5)	1.0(−4)	...	...	1.8(−2)
Pure iron	2.0(−4)	...	...	...	...	...	...	2.0(−4)
Iron sulfide	5.4(−8)	...	...	...	...	...	...	5.4(−8)
Pure silicon	3.6(−4)	...	...	...	...	...	...	3.6(−4)
Pure magnesium	...	...	9.9(−4)	...	...	...	...	9.9(−4)
Carbon	...	...	...	...	...	5.5(−3)	...	5.5(−3)
Silicon carbide	...	...	...	...	...	2.6(−4)	...	2.6(−4)
Total mass ( $M_{\odot}$ )	5.6(−4)	2.0(−3)	2.6(−2)	1.9(−4)	3.5(−4)	5.8(−3)	0	0.035
Efficiency	0.51%	0.66%	1.6%	0.13%	7.2(−2)%	0.71%	0%	0.91%

**Note.** Efficiencies are the molecule or dust-to-gas mass ratio in each zone and for the total ejected zones of the He core.

in a larger molecular component and dust cluster formation efficiency in the ejecta, as seen from Table 4. Most importantly, the impact of reducing the  $^{56}\text{Ni}$  mass anticipates the formation of forsterite clusters at as early as 250 days in zone 2. These clusters may not coalesce readily into silicate grains because the gas temperature is still high ( $\sim 2300$  K) at day 300, but the efficient formation of silicate clusters results in changing final dust cluster compositions at late times—see Table 4 and Figure 8. The dust budget now includes 45.0% forsterite, 41.4% carbon, and 13.6% alumina, as opposed to 60% carbon, 20% alumina, 15% forsterite, and a few % pure metal clusters for the standard case of Section 3.1.2.

### 3.3. 19 and 25 $M_{\odot}$ Progenitors

We now present the results for the ejecta chemistry associated with a  $19 M_{\odot}$  progenitor. The initial composition of the ejecta is given in Table 1 and the chemistry for all zones is identical to that considered for the standard model. All results for the masses of molecules and dust are summarized in Table 6. The masses of CO and SiO formed over the time span 100–1500 days are shown in Figure 10. The evolution of both molecules with post-explosion time resembles that of the  $15 M_{\odot}$  case. The formation of CO commonly occurs in zones 3 and 4, which correspond to zones 4A and 4B of the  $15 M_{\odot}$  progenitor. These zones are not efficient at forming dust, as seen in Table 6. As for the  $15 M_{\odot}$  case, the conclusion that CO does not trace carbon dust formation in the ejecta holds for the  $19 M_{\odot}$  progenitor. Likewise, the variation of SiO masses with time shows similar trends as for the standard model, the only exception being zone 2. Indeed, the destruction of SiO prevails at early times owing to the high Ne content of the zone, as seen in Table 1, that results in high  $\text{Ne}^+$  masses at early times. The chemical trends for the formation and destruction of O<sub>2</sub> and SO are also akin to those already described in Section 3.1.1. More generally, the

total mass of molecules produced by the  $19 M_{\odot}$  progenitor is higher by a factor of  $\sim 2$  compared with the  $15 M_{\odot}$  case, but the efficiencies of forming molecules for the two cases are similar. About 30% of the material ejected by an SN with a progenitor mass of  $15$ – $19 M_{\odot}$  is in molecular form.

In Figure 11, we show cluster mass evolution as a function of time for the  $19 M_{\odot}$  progenitor. The FeS clusters are the first to form in zone 1A with a small mass compared with pure iron clusters (see Table 6). Furthermore, the FeS mass is smaller than that derived by Cherchneff & Dwek (2010) for the  $20 M_{\odot}$  progenitor with zero metallicity. This discrepancy arises from the larger Fe/S yields characterizing the innermost zones of the primeval  $20 M_{\odot}$  progenitor. Forsterite clusters experience two phases of growth. The first phase, between 200 and 500 days, is characterized by a forsterite mass reaching a value of  $\sim 5 \times 10^{-4} M_{\odot}$  at 300 days. Zone 1B is responsible for this early growth event owing to the first production event of SiO at day 200 seen in Figure 10. A second forsterite growth event occurs around day 700, corresponding to the peak in SiO formation in zone 2 at this time. The composition of the grains is shown in Figure 8. The prevalent dust formed is alumina, followed by forsterite, carbon, and finally some Mg dust. Despite similarities between the chemical processes at play in the formation and destruction of molecules and dust in the ejecta and similar upper limit values on the final dust mass at day 1500, the variation in the dust composition between the  $15 M_{\odot}$  and the  $19 M_{\odot}$  progenitors reflects the initial chemical composition of the ejecta given by the explosion nucleosynthesis models.

We now consider the ejecta of a  $25 M_{\odot}$  progenitor with a high  $^{56}\text{Ni}$  mass ( $0.075 M_{\odot}$ ), a surrogate for the explosion of a massive star like the progenitor of SN2004et or the explosion of population II supergiant stars at high redshift, metallicity notwithstanding. The cluster masses versus post-explosion times are shown in Figure 11 and the molecule and

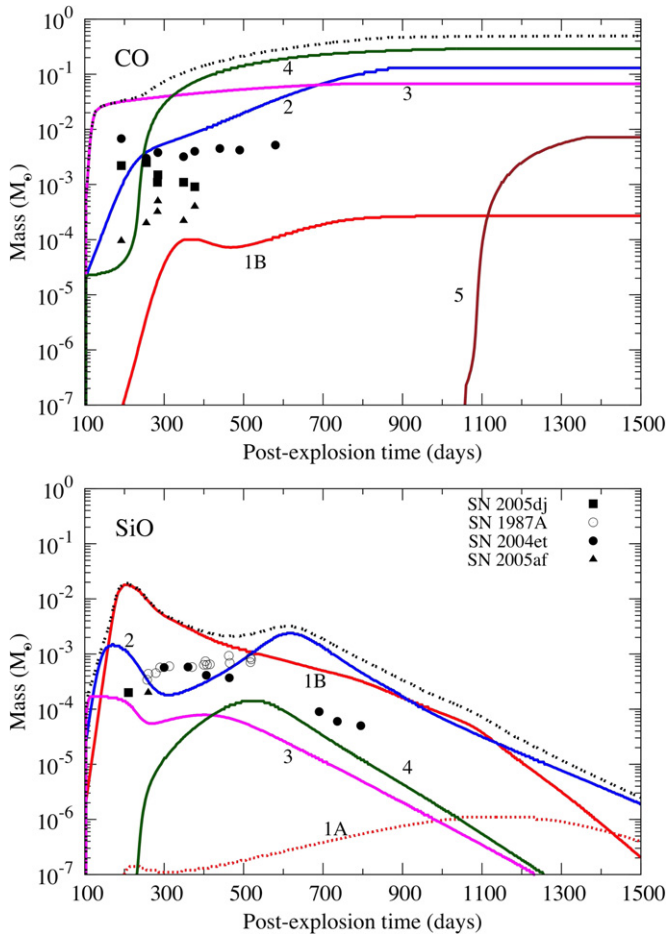


**Figure 10.** Top: CO mass as a function of post-explosion time for the  $19 M_\odot$  progenitor for the various ejecta zones (see Table 1 for zone labeling). CO masses derived for SN1987A are also shown—see Figure 2 for details. Bottom: SiO mass evolution with post-explosion time for the  $19 M_\odot$  progenitor. The masses derived for several SNe are also shown as symbols. The dotted gray line represents the mass summed over all zones.

(A color version of this figure is available in the online journal.)

cluster masses as a function of ejecta zoning are listed in Table 7. The synthesis of clusters starts at day 200 with a rapid increase in the forsterite mass that reaches  $6 \times 10^{-3} M_\odot$  at day 400 and  $6 \times 10^{-2} M_\odot$  at 700 days. As seen from Table 1, a large oxygen and silicon content characterizes the oxygen core in zones 2 and 3 of the  $25 M_\odot$  progenitor and triggers an efficient silicate cluster synthesis. The large aluminum and oxygen yields characterizing zone 3 guarantee the formation of a large mass of AlO, the molecular precursor to  $\text{Al}_2\text{O}_3$ . However, the large Ne yield of the zone results in a large  $\text{Ne}^+$  abundance that delays the formation of AlO to day 750. Table 1 also indicates a large fraction of carbon compared with oxygen ( $\text{C/O} \sim 36$ ), accompanied by a large yield of helium in zone 5. Such a composition results in the delayed formation of carbon and silicon carbide clusters in this zone after day 1500 owing to the large fraction of  $\text{He}^+$  in the zone. As illustrated in Figure 8, the  $25 M_\odot$  progenitor primary forms alumina and forsterite clusters, while carbon dust is a very minor component of the condensates formed by these massive SNe.

To conclude, SNe with large progenitor masses tend to form dust with efficiencies similar to that of the standard  $15 M_\odot$  progenitor, but are more efficient at forming molecules. The molecular component of the ejecta can be as large as  $\sim 50\%$  of the total ejected mass. The larger the progenitor mass, the

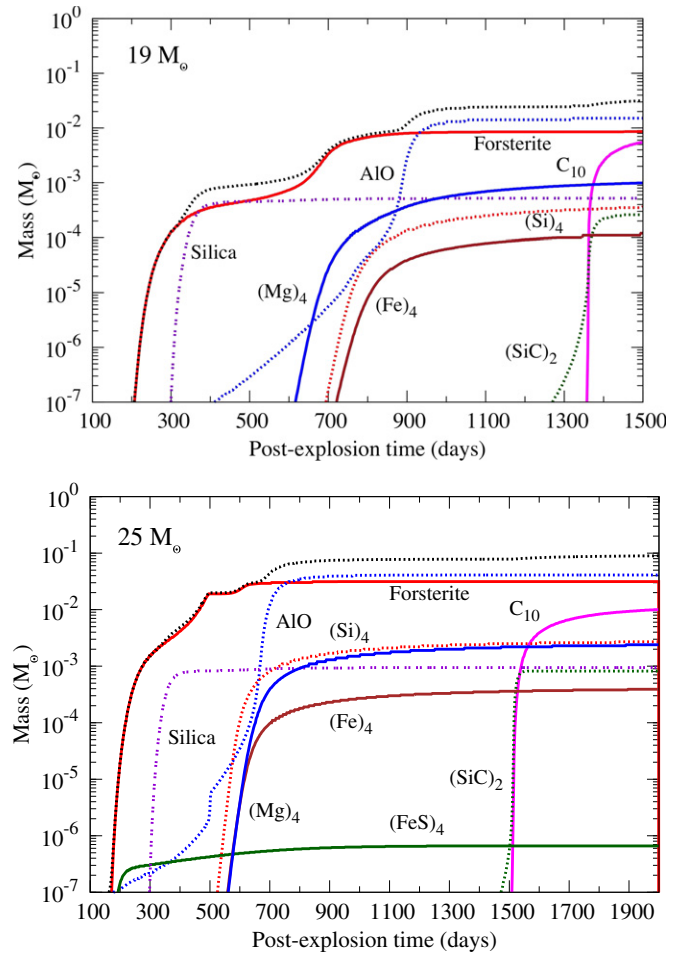


**Figure 11.** Top: the evolution of dust cluster masses with post-explosion time for the  $19 M_\odot$  progenitor. Bottom: dust mass for the  $25 M_\odot$  progenitor as a function of post-explosion time for a  $^{56}\text{Ni}$  mass of  $0.075 M_\odot$ . For each cluster type, the masses have been summed over all zones of the ejecta. The dotted gray line represents the total cluster mass and provides an upper limit on the mass of dust that forms in the ejecta.

(A color version of this figure is available in the online journal.)

later carbon clusters form owing to the large  $\text{He}^+$  content in the outermost ejecta zone. At late times, the decrease in gas number densities may hamper the efficient condensation of carbon chains in AC dust. In the end, these massive progenitors produce a small mass of carbon clusters that may not totally transform into dust, but should chiefly synthesize O-rich condensates (e.g., silicates and alumina) in their ejecta.

### 3.4. $12 M_\odot$ Progenitor with a Low $^{56}\text{Ni}$ Mass

As shown from Table 5, low-mass progenitors tend to produce low  $^{56}\text{Ni}$  masses in contrast with large-mass progenitors. We thus model the ejecta of a  $12 M_\odot$  progenitor with a small  $^{56}\text{Ni}$  mass ( $0.01 M_\odot$ ) that can be regarded as a template for low-energy, faint SNe. Another SN environment originating from a low-mass progenitor includes the Crab Nebula, an SNR resulting from the explosion of a supergiant with mass  $\sim 10 M_\odot$  (Davidson & Fesen 1985; MacAlpine & Satterfield 2008). The molecule and cluster masses as a function of ejecta zoning for the  $12 M_\odot$  progenitor are given in Table 8. In general, trends similar to those for other progenitor masses are obtained, i.e., the ejecta produces a large fraction of molecules ( $\sim 20\%$  by mass). The ejecta zone most efficient at producing species, including CO and  $\text{O}_2$ , corresponds to the O- and C-rich outer zone of the



**Table 7**Masses of Molecules and Upper Limits on Dust Masses (Both in  $M_{\odot}$ ) at 2000 Days for the 25  $M_{\odot}$  Progenitor with a  $^{56}\text{Ni}$  Mass of 0.075  $M_{\odot}$ 

Ejected Zones	Zone 1A	Zone 1B	Zone 2	Zone 3	Zone 4A	Zone 4B	Zone 5	Zone 6	Total
Zone mass ( $M_{\odot}$ )	0.233	0.181	0.463	2.72	0.526	0.89	0.956	0.236	6.21
Major elements	Si/S/Fe	Si/O/S	O/Mg/Si	O/Ne/Mg	O/C	He/O/C	He/C	He/N	
Molecules									
SiO	5.5(−8)	2.3(−7)	1.3(−7)	1.2(−6)	2.5(−7)	3.9(−7)	...	...	2.2(−6)
O <sub>2</sub>	...	...	0.10	1.4	0.18	7.5(−2)	...	...	1.76
CO	...	2.0(−5)	2.1(−4)	7.9(−2)	0.24	0.54	7.6(−4)	...	0.86
SO	...	1.9(−7)	5.6(−2)	1.2(−2)	2.7(−4)	...	...	...	6.8(−2)
SiS	0.12	1.6(−2)	1.5(−6)	...	...	...	...	...	0.1
Total mass ( $M_{\odot}$ )	0.12	1.6(−2)	0.156	1.49	0.42	0.62	7.6(−4)	0	2.82
Efficiency(%)	51.5%	8.9%	33.6%	54.8%	79.8%	70.7%	7.9(−2)%		45.4%
Dust									
Forsterite—Mg <sub>2</sub> SiO <sub>4</sub>	...	1.6(−5)	1.9(−2)	1.2(−2)	1.1(−4)	1.8(−4)	...	...	3.2(−2)
Silica—SiO <sub>2</sub>	...	...	3.1(−4)	6.0(−4)	...	...	...	...	9.1(−4)
Alumina—Al <sub>2</sub> O <sub>3</sub>	...	1.3(−3)	3.9(−2)	1.3(−4)	2.6(−4)	3.5(−5)	...	...	4.1(−2)
Pure iron—Fe	5.7(−4)	...	...	...	...	...	...	...	5.7(−4)
Iron sulfide—FeS	6.6(−7)	...	...	...	...	...	...	...	6.6(−7)
Pure silicon—Si	2.5(−3)	...	...	...	...	...	...	...	2.5(−3)
Pure magnesium—Mg	...	...	...	2.2(−3)	...	...	...	...	2.2(−3)
Carbon—C <sub>10</sub>	...	...	...	...	...	...	1.0(−2)	...	1.0(−2)
Silicon carbide - SiC	...	...	...	...	...	...	8.2(−4)	...	8.2(−4)
Total mass ( $M_{\odot}$ )	3.1(−3)	1.4(−3)	5.8(−2)	1.5(−2)	3.7(−4)	2.2(−4)	1.1(−3)	0	0.09
Efficiency	1.33%	0.77%	12.5%	0.55%	7.0(−2)%	2.5(−2)%	0.11%		1.3%

**Note.** Efficiencies are the molecule or dust-to-gas mass ratio in each zone and for the total ejected zones of the He core.**Table 8**Masses of Molecules and Upper Limits on Dust Masses (Both in  $M_{\odot}$ ) at 1500 Days for the 12  $M_{\odot}$  Progenitor with a  $^{56}\text{Ni}$  Mass of 0.01  $M_{\odot}$ 

Ejected Zones	Zone 1A	Zone 1B	Zone 2	Zone 3	Zone 4	Zone 5	Total
Zone mass ( $M_{\odot}$ )	6.1(−2)	0.13	0.14	0.16	0.16	0.92	1.57
Major elements	Si/S/Fe	Si/O	O/Ne/Mg	O/C	He/C	He/N	
Molecules							
SiO	3.0(−8)	5.7(−8)	6.0(−8)	7.0(−8)	...	...	2.2(−7)
O <sub>2</sub>	...	6.8(−2)	6.4(−2)	4.9(−2)	...	...	0.18
CO	2.4(−7)	6.5(−5)	1.2(−3)	7.0(−2)	5.5(−3)	...	7.7(−2)
SO	...	3.9(−3)	6.2(−5)	5.5(−9))	...	...	4.0(−3)
SiS	4.7(−2)	...	...	...	...	...	4.7(−2)
Total mass ( $M_{\odot}$ )	4.7(−2)	7.2(−2)	6.5(−2)	0.12	5.5(−3)	0	0.31
Efficiency	77%	55.4%	46.4%	75%	3.4%		19.7%
Dust							
Forsterite—Mg <sub>2</sub> SiO <sub>4</sub>	...	1.2(−2)	2.9(−4)	2.2(−4)	...	...	1.3(−2)
Enstatite—MgSiO <sub>3</sub>	...	...	...	...	...	...	...
Silica—SiO <sub>2</sub>	...	5.2(−6)	5.0(−6)	...	...	...	1.2(−5)
Alumina—Al <sub>2</sub> O <sub>3</sub>	...	7.9(−4)	1.03(−3)	3.9(−4)	...	...	2.2(−3)
Pure iron—Fe	2.3(−5)	...	...	...	...	...	2.3(−5)
Iron sulfide—FeS	1.0(−7)	...	...	...	...	...	1.0(−7)
Pure silicon—Si	8.3(−5)	...	...	...	...	...	8.3(−5)
Pure magnesium—Mg	...	8.1(−6)	1.6(−4)	...	...	...	1.7(−4)
Carbon—C <sub>10</sub>	...	...	...	...	3.3(−2)	...	3.3(−2)
Silicon carbide—SiC	...	...	...	...	5.0(−6)	...	5.0(−6)
Total mass ( $M_{\odot}$ )	1.1(−4)	1.3(−2)	1.5(−3)	6.1(−4)	3.3(−2)	0	0.048
Efficiency	0.2%	10%	1.1%	0.4%	20.6%		3.1%

**Note.** Efficiencies are the molecule or dust-to-gas mass ratio in each zone and for the total ejected zones of the He core.

oxygen core (labeled zone 3), characterized by a C/O ratio with a typical value of 0.3. For the 12  $M_{\odot}$  progenitor, the innermost zone, zone 1A, is also very efficient at producing SiS because of the large initial Si and S yields and the low Fe yield, as seen

in Table 1. Essentially all atomic S gets trapped in SiS in this zone.

As for dust, cluster masses versus post-explosion times are shown in Figure 12. As discussed in Section 3.2, the

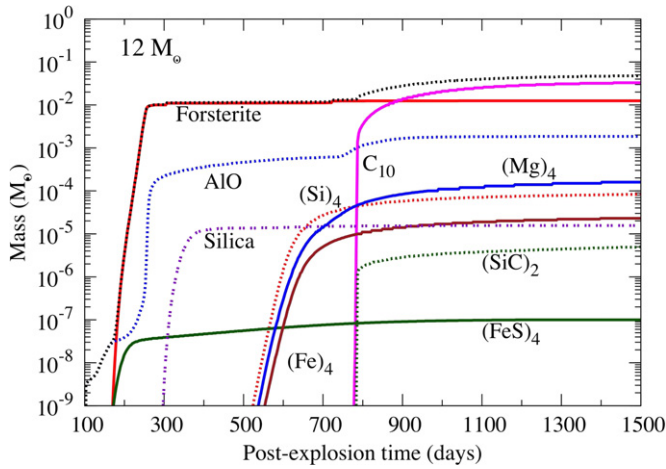


**Figure 12.** Evolution of dust cluster masses with post-explosion time for the  $12 M_{\odot}$  progenitor with a  $^{56}\text{Ni}$  mass of  $0.01 M_{\odot}$ . For each cluster type, the masses have been summed over all zones of the ejecta. The dotted gray line represents the total cluster mass and provides an upper limit on the mass of dust that forms in the ejecta.

(A color version of this figure is available in the online journal.)

formation of forsterite clusters occurs as early as 250 days post-explosion owing to the low  $^{56}\text{Ni}$  ejecta content. However, the gas temperature at day 250 is too high ( $\sim 2500$  K) to permit the coalescence of forsterite clusters in silicate dust. This process will take place once the gas temperature reaches  $\sim 1500$  K around day 400. However, for this progenitor, the onset of AlO formation also occurs around day 250. Alumina,  $\text{Al}_2\text{O}_3$ , being more refractory than silicates, may then precede the formation of forsterite between 250 and 300 days, leading to the early formation of  $\text{Al}_2\text{O}_3$  dust in the ejecta, followed by a forsterite dust formation event. As for the  $15 M_{\odot}$  low  $^{56}\text{Ni}$  case, the synthesis of carbon chains and rings is also shifted to an earlier epoch,  $\sim 800$  days, implying that AC grains will form more efficiently in low-mass SN progenitors because of the larger gas densities. A  $12 M_{\odot}$  model should thus lead to a dust formation time sequence of  $\text{Al}_2\text{O}_3$ , silicates, AC, where in the end, carbon represents  $\sim 68\%$ , silicate  $\sim 28\%$ , and alumina  $\sim 6\%$  of the total dust mass, respectively, as seen from Figure 8.

A dust formation event before 200 days, possibly involving alumina as a first condensate, should then characterize SN progenitors with masses smaller than  $12 M_{\odot}$  and low  $^{56}\text{Ni}$  masses. Such an early dust formation episode is observed in some SNe with low-mass progenitors, e.g., SN2011ht (Mauerhan et al. 2012), and is often ascribed to the interaction of the explosion blast wave with the dense progenitor wind at early epochs. A dense shell conducive to dust condensation forms in the post-shock region, resulting in a dust production episode. The present results indicate that the early formation of dust may also be due to a low  $^{56}\text{Ni}$  mass in the ejecta. Hence, the observed early condensation episode in faint SNe may arise from a combination of both scenarios.

### 3.5. Elements

Sections 3.1.1 and 3.1.2 highlighted the importance of the molecular and dust components of SN ejecta that amount to 30%–50% of the ejecta mass depending on the progenitor mass. The rest of the ejecta is in the form of atomic elements, either neutrals or ions. The masses of elements as a function of post-explosion time are shown in Figure 13 for the standard case. The top figure illustrates the masses summed over all ejecta

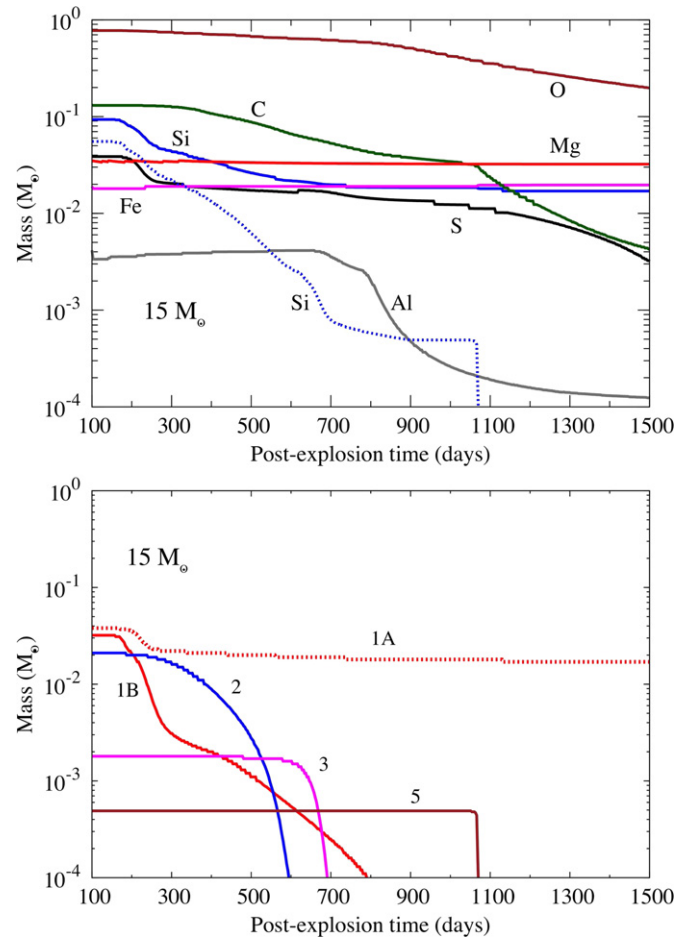


**Figure 13.** Top: the evolution of element masses summed over all ejecta zones with post-explosion time for the  $15 M_{\odot}$  progenitor. The dotted blue line represents the Si mass resulting from all zones except for the innermost zone (zone 1A). Bottom: atomic silicon mass for the  $15 M_{\odot}$  progenitor as a function of ejecta zones and post-explosion time. Si atoms are rapidly depleted in the formation of SiO, silica, and silicate clusters in most of the zones except for zone 1A, where Si is primarily depleted in SiS.

(A color version of this figure is available in the online journal.)

zones versus time, while the bottom figure focuses on atomic Si mass variation versus time for each zone. Until day  $\sim 800$ , most elements including O, Mg, Fe, and Al show almost constant masses in the ejecta. After day 800, O and Al masses decrease owing to the formation of AlO in the O-rich core of the ejecta. The mass of atomic carbon shows a small decrease after day 300 due to the formation of CO in most of the zones, and a sharper decline after day 1050 resulting from the formation of carbon chains and rings in zone 5. The overall atomic silicon mass slightly decreases over time until it reaches a constant mass at day  $\sim 700$ . This mass variation primarily reflects zone 1A where the large Si content is depleted at early epochs in the formation of SiS (see Figure 2). The Si dotted line in the top figure depicts the Si mass summed over all zones except for zone 1A. These zones include the oxygen-rich core of the ejecta (zones 1B, 2, and 3) where most of the silica and silicate clusters form. The summed Si mass shows a sharp decline between  $\sim 200$  and 800 days that reflects the depletion of Si in the formation of SiO, silica, and silicates in zones 1B, 2, and 3, between day 200 and day 700.

As first shown by Lucy et al. (1989) for SN1987A, the fluxes of the [O I] 6300 Å and [Mg I] 4571 Å emission lines faded with time, with a sharper decline at day  $\sim 530$ , indicative of the

onset of dust formation. The [Si I] emission line at  $1.6445\ \mu\text{m}$  showed a markedly stronger fading relative to the continuum that pinpointed either a decrease in the Si abundance owing to dust condensation or temperature effects induced by strong cooling in the Si zone. A similar fading of the Mg and O line fluxes from day 500 until day 800 observed by Lucy et al. indicates that extinction induced by dust condensation around day 500 was responsible for the fading. This interpretation is supported by the present calculations, as both elements show a time-independent mass evolution over this time span. On the other hand, the sharper fading observed in the Si emission line flux probably ensues from the combined effects of extinction and Si depletion in SiO and dust grains, as illustrated in Figure 13.

### 3.6. Comparison with Existing Studies

Several studies have tackled the modeling of dust formation in Type II-P SNe. The first attempt to model the synthesis of grains in SN1987A was carried out by Kozasa et al. (1989). Later studies dealt with the formation of dust in Type II-P SNe locally (Bianchi & Schneider 2007) and at high redshift (Todini & Ferrara 2001; Nozawa et al. 2003). All these studies consider the formation of dust grains from the gas phase using classical nucleation theory (CNT). Some assume fully mixed ejecta (Todini & Ferrara 2001; Bianchi & Schneider 2007), while others consider stratified ejecta (Kozasa et al. 1989, 2009; Nozawa et al. 2003). A few studies consider the impact of the steady-state formation of CO and SiO from the gas phase, including the destruction of CO by Compton electrons, on the final carbon and silicate dust masses (Todini & Ferrara 2001; Bianchi & Schneider 2007). This assumption gives rise to the formation of carbon dust in fully mixed ejecta with a C/O ratio less than 1, a result that contradicts the findings of Kozasa et al. (1989).

All existing CNT-based models for the progenitor masses of interest in the present study are summarized in Table 9, with the derived dust masses and the modeled dust condensation sequences over time. CNT-derived dust masses for solar metallicity ejecta have values higher by a factor of  $\sim 10$  compared with the upper limits of dust masses derived in this study. This discrepancy follows from several assumptions. First, several models (Todini & Ferrara 2001; Bianchi & Schneider 2007) consider fully mixed ejecta. Such a scenario is not confirmed by explosion hydrodynamic models (Hammer et al. 2010) and observations of SNRs, which point to the memory of nucleosynthesis layers within the remnant, as in Cas A (Isensee et al. 2012). Because the dust mass is derived from the total elemental yields and chemistry is not properly considered, fully mixed ejecta always produce larger dust quantities. Second, in unmixed models, CNT is applied to steady-state conditions that are usually not found in the dynamic environments characterizing SN ejecta. Finally, all CNT-based models ignore the non-equilibrium chemistry related to the formation of molecules and dust clusters and the specific physics of SN ejecta where radioactivity greatly impacts the gas-phase chemistry through Compton electron ionization.

These specificities also affect the dust condensation sequence, as seen in Table 9. In CNT-based studies, the condensation sequence is derived assuming equilibrium temperature and pressure as initial conditions. In the present study, the dust condensation sequences ensue from non-equilibrium chemical kinetics and thus depend on ejecta parameters such as the initial post-explosion elemental yields, the mass of  $^{56}\text{Ni}$  produced, and the gas temperature and density. This fact is well illustrated

by the 15, 19, and  $25\ M_{\odot}$  progenitors, for which silicate clusters form before the molecule AlO, when alumina,  $\text{Al}_2\text{O}_3$ , is supposed to be the first solid to condense in O-rich environments at thermodynamic equilibrium (Tielens et al. 1998). Here,  $\text{Mg}_2\text{SiO}_4$  production precedes that of  $\text{Al}_2\text{O}_3$  because of the early destruction of AlO molecules by  $\text{Ne}^+$  ions in the gas.

More generally, existing studies based on CNT overestimate the total dust mass formed in SN ejecta. Dust formation sequences assuming thermodynamic equilibrium are very commonly used as benchmarks in the modeling of dust synthesis in O-rich evolved stellar media, but should be avoided when modeling stellar outflows and ejecta where dynamics and chemistry control the synthesis of condensates.

## 4. SUMMARY AND DISCUSSION

We have investigated the synthesis of molecules and dust clusters in stratified ejecta of Type II-P SNe with solar metallicity. Our results highlight the following points.

1. Molecules including SiS, CO,  $\text{O}_2$ , and SO represent a large fraction of the gas-phase ejecta ( $\sim 30\%$  by mass). Specifically, the CO mass increases from  $10^{-4}$  at 100 days and gradually reaches  $\sim 0.1\ M_{\odot}$  1500 days post-explosion for all SN progenitors. This high CO mass forms in an ejecta zone where carbon dust does not condense, suggesting that most of the observed CO does not trace the carbon dust formation process in SN ejecta.
2. The molecule SiO efficiently forms at an early epoch and is quickly converted into SiO dimers and silica and silicate clusters. The mass of SiO at day 1500 is  $\sim 10^{-6}\ M_{\odot}$  or less. SiO is thus a direct tracer of dust formation in SN ejecta.
3. The dust clusters form at different post-outburst epochs in various zones. Silicate clusters experience a delayed formation owing to the early destruction of  $\text{O}_2$  and SO. The growth of silicate clusters via oxygen addition then occurs at  $\sim$ day 500 for our standard case. Carbon chains and rings and silicon carbide clusters form in the outermost zone of the He cores and at late times owing to the detrimental attack of  $\text{He}^+$  on molecules. In more general terms, the dust mass gradually increases over time from  $\sim 10^{-5}\ M_{\odot}$  at 400 days to  $\sim 0.03\text{--}0.09\ M_{\odot}$  after day 1500. This gradual synthesis of dust clusters over a time span of  $\sim 4$  yr provides a plausible explanation for the discrepancy observed between the dust masses derived from IR observations at early epochs and the larger masses of cool dust observed at submm wavelengths in SNRs.
4. The formation of dust clusters occurs according to a sequence of condensation events at various epochs. Low-mass progenitors experience anticipated dust formation events of essentially carbon dust with a minor silicate and alumina component, owing to the small masses of  $^{56}\text{Ni}$  in the ejecta. High-mass progenitors primarily form silicates and alumina dust, with a minor component of carbon dust. Compared with existing models of dust synthesis in Type II-P SNe based on CNT, our results indicate masses of synthesized dust that are smaller by a factor of  $\sim 10$  and different dust condensation sequences and chemical compositions.

The large fraction of the material expelled in an SN event is in molecular form ( $\sim 20\%\text{--}50\%$ ) with a chemical composition including SiS, CO,  $\text{O}_2$ , and SO, depending on zoning. These four chemical species will pervade the late stages of SN evolution, i.e., the SNR not yet hit by the reverse shock. Evidence for

**Table 9**  
Condensation Time Sequence and Dust Mass Derived by Existing Dust Formation Models for  $Z = Z_{\text{solar}}$  and  $Z = 0$  Metallicity<sup>a</sup>

Model	Z	Fully Mixed or Unmixed	Progenitor Mass	Dust Condensation Time Sequence	Total Dust Mass
Kozasa et al. (1989)	Solar	FM	19 $M_{\odot}$	$\text{Al}_2\text{O}_3\text{--Mg}_2\text{SiO}_4\text{--Fe}_3\text{O}_4$	...
	Solar	U	19 $M_{\odot}$	Graphite	...
Kozasa et al. (2009)	Solar	U	15 $M_{\odot}$	AC– $\text{Al}_2\text{O}_3\text{--Mg}_2\text{SiO}_4$ and $\text{MgSiO}_3\text{--SiO}_2\text{--Fe}_3\text{O}_4\text{--MgO--Si--FeS--Fe}$	0.33 $M_{\odot}$
	Solar	U	20 $M_{\odot}$	...	0.68 $M_{\odot}$
Todini & Ferrara (2001)	Solar	FM	12 $M_{\odot}$	...	0.20 $M_{\odot}$
	Solar	FM	15 $M_{\odot}$	...	0.45 $M_{\odot}$
	Solar	FM	20 $M_{\odot}$	AC– $\text{Al}_2\text{O}_3\text{--Fe}_3\text{O}_4\text{--Mg}_2\text{SiO}_4\text{--MgSiO}_3$	0.70 $M_{\odot}$
	Solar	FM	25 $M_{\odot}$	...	1.00 $M_{\odot}$
	0	FM	15 $M_{\odot}$	AC– $\text{Al}_2\text{O}_3\text{--Fe}_3\text{O}_4\text{--Mg}_2\text{SiO}_4\text{--MgSiO}_3$	0.45 $M_{\odot}$
	0	FM	20 $M_{\odot}$	AC	0.08 $M_{\odot}$
	0	FM	25 $M_{\odot}$	AC	0.08 $M_{\odot}$
Nozawa et al. (2003)	0	FM	20 $M_{\odot}$	$\text{Al}_2\text{O}_3\text{--Mg}_2\text{SiO}_4\text{--SiO}_2\text{--Fe}_3\text{O}_4$	0.73 $M_{\odot}$
	0	U	20 $M_{\odot}$	AC– $\text{Al}_2\text{O}_3\text{--Mg}_2\text{SiO}_4\text{--MgO--SiO}_2\text{--Si--FeS--Fe}$	0.57 $M_{\odot}$
Bianchi & Schneider (2007)	Solar	FM	12 $M_{\odot}$	...	0.12 $M_{\odot}$
	Solar	FM	15 $M_{\odot}$	...	0.28 $M_{\odot}$
	Solar	FM	20 $M_{\odot}$	AC– $\text{Al}_2\text{O}_3\text{--Mg}_2\text{SiO}_4\text{--SiO}_2\text{--Fe}_3\text{O}_4\text{--MgSiO}_3$	0.40 $M_{\odot}$
	Solar	FM	25 $M_{\odot}$	...	0.62 $M_{\odot}$
Cherchneff & Dwek <sup>b,c</sup> (2010)	0	FM	20 $M_{\odot}$	Mg–Si/Fe– $\text{SiO}_2\text{--Al}_2\text{O}_3$	0.16 $M_{\odot}$
	0	U	20 $M_{\odot}$	$\text{Al}_2\text{O}_3\text{--SiO}_2\text{--MgO--FeS--Si--Mg/Fe--AC}$	0.10 $M_{\odot}$
Sarangi & Cherchneff <sup>b</sup> (this paper)	Solar	U	12 $M_{\odot}$	$\text{Al}_2\text{O}_3\text{--Mg}_2\text{SiO}_4\text{--SiO}_2\text{--Si/Mg/Fe--AC/SiC}$	0.048 $M_{\odot}$
	Solar	U	15 $M_{\odot}$	$\text{Mg}_2\text{SiO}_4\text{/SiO}_2\text{--FeS--Al}_2\text{O}_3\text{--Si--Fe--AC/SiC}$	0.038 $M_{\odot}$
	Solar	U	19 $M_{\odot}$	$\text{Mg}_2\text{SiO}_4\text{--SiO}_2\text{--Mg--Si--Fe--Al}_2\text{O}_3\text{--AC/SiC}$	0.035 $M_{\odot}$
	Solar	U	25 $M_{\odot}$	$\text{Mg}_2\text{SiO}_4\text{--SiO}_2\text{--Si--Al}_2\text{O}_3\text{--FeS--Fe/Mg--AC/SiC}$	0.09 $M_{\odot}$

#### Notes.

<sup>a</sup> Dust condensation time sequences are only available from the literature for a set of progenitor masses.

<sup>b</sup> The dust mass is derived assuming 100% condensation of the dust clusters in grains. Mass values are then upper limits on the total dust masses that form in the ejecta.

<sup>c</sup> The formation of forsterite and entastite is not modeled.  $\text{SiO}_2$  represents the generic class of silicates.

molecules in SNRs was presented by the detection of the first overtone transition of CO in the young remnant Cas A (Rho et al. 2009). The fundamental band at  $4.56 \mu\text{m}$  was subsequently observed with *AKARI* (Rho et al. 2012). As already proposed by Cherchneff & Sarangi (2011), our results strongly suggest that a large fraction of cool CO ( $\sim 0.1 M_{\odot}$ ) formed in the ejecta should pervade the remnant gas not yet shocked by the reverse shock and thus be detectable. The recent detection with ALMA of cool CO formed in the ejecta of SN1987A with a derived mass  $\geq 0.1 M_{\odot}$  confirms our present results (Kamenetsky et al. 2013). Most interesting are the large masses of SiS ( $0.04\text{--}0.1 M_{\odot}$ ) formed in the innermost zone of SN ejecta. Emission line analysis of SNRs suggests that the remnant has retained some memory of the ejecta stratification due to nucleosynthesis, consistent with explosion models (Chevalier & Kirschner 1978; Fesen et al. 2006; DeLaney et al. 2010; Isensee et al. 2012; Ghavamian et al. 2012). If so, SiS molecules should exist in the Cas A remnant in sulfur, silicon, and calcium-rich fast moving knots, and possibly be detectable there at submm wavelengths.

The present results on molecules may put constraints on the physical parameters of the ejecta. The formation of SiO dimers is a good example. The SiO dimer formation rate is gas pressure-dependent and usually very low at the low pressures encountered in the ejecta before day 400. When the SiO dimerization rate derived by Zachariah & Tsang (1993) is used for the ejecta pressure, SiO and subsequent forsterite dimer formation is postponed to late epochs ( $t > 700$  days), as shown by Cherchneff & Dwek (2010) for primeval, massive

SN explosions. In the present models, the SiO dimerization rate has been increased to account for the density enhancement found in clumps and the match between SiO observational data and modeled masses is satisfactory (see Figure 4). We conclude that the observed SiO line fading and the timing for dust condensation are thus indirect indicators of the clumpy nature of SN ejecta.

The upper limit on dust mass produced by our sample of SNe spans the  $0.03\text{--}0.09 M_{\odot}$  range. These values are much larger than those derived from IR data but somewhat less than the values derived from submm data, i.e.,  $0.4\text{--}0.7 M_{\odot}$  for SN1987A and  $0.24 M_{\odot}$  for the Crab Nebula. However, these large masses have been derived assuming a simple dust composition (usually, either carbon or silicate with the addition of some iron) and restricted physical parameters (i.e., one or two dust temperatures). The chemistry of dust synthesis has not been considered and condensing efficiencies of 100% of all available elements are usually assumed (e.g., Matsuura et al. 2011). All of these factors tend to boost the mass of solids synthesized in SN ejecta, when lower dust masses should be expected due to the bottleneck effect of the nucleation phase and the large variety of condensates produced in the gas. To validate our modeled dust chemical compositions, masses, and formation sequences, a study on the modeling of IR and submm fluxes for the homogeneous and clumpy ejecta of several SNe and SNRs will be presented in a forthcoming paper.

The possibility of new formation of grains and their growth at late epochs ( $t > 5$  yr) in the ejecta must be addressed. First,



**Table 10**  
The Chemical Routes to Nucleation of the Various Clusters Considered in the Present Study<sup>a</sup>

Reaction	Reactants		Products	$A_{ij}$	$\nu$	$E_a$	References <sup>b</sup>
(SiO) <sub>n</sub> clusters							
A1	SiO+SiO	→	Si <sub>2</sub> O <sub>2</sub>	$4.6086 \times 10^{-17}$	0	−2821.4	ZT93, CD10
A2	Si <sub>2</sub> O <sub>2</sub> +SiO	→	Si <sub>3</sub> O <sub>3</sub>	$2.2388 \times 10^{-15}$	0	−2878.9	”
A3	Si <sub>2</sub> O <sub>2</sub> + Si <sub>2</sub> O <sub>2</sub>	→	Si <sub>3</sub> O <sub>3</sub> +SiO	$1.5265 \times 10^{-14}$	0	−2386.8	”
A4	Si <sub>3</sub> O <sub>3</sub> +SiO	→	Si <sub>4</sub> O <sub>4</sub>	$1.5265 \times 10^{-14}$	0	−2386.8	”
A5	Si <sub>2</sub> O <sub>2</sub> + Si <sub>2</sub> O <sub>2</sub>	→	Si <sub>4</sub> O <sub>4</sub>	$1.5265 \times 10^{-14}$	0	−2386.8	”
A6	Si <sub>3</sub> O <sub>3</sub> + Si <sub>2</sub> O <sub>2</sub>	→	Si <sub>4</sub> O <sub>4</sub> +SiO	$1.5265 \times 10^{-14}$	0	−2386.8	”
A7	Si <sub>4</sub> O <sub>4</sub> +SiO	→	Si <sub>5</sub> O <sub>5</sub>	$1.5265 \times 10^{-14}$	0	−2386.8	”
A8	Si <sub>3</sub> O <sub>3</sub> + Si <sub>2</sub> O <sub>2</sub>	→	Si <sub>5</sub> O <sub>5</sub>	$1.5265 \times 10^{-14}$	0	−2386.8	”
A9	Si <sub>2</sub> O <sub>2</sub>	→	SiO+SiO	$7.7200 \times 10^{-7}$	0	0	”
A10	Si <sub>3</sub> O <sub>3</sub>	→	Si <sub>2</sub> O <sub>2</sub> +SiO	$7.8300 \times 10^{-6}$	0	0	”
A11	Si <sub>4</sub> O <sub>4</sub>	→	Si <sub>3</sub> O <sub>3</sub> +SiO	$9.9000 \times 10^{-4}$	0	0	”
A12	Si <sub>4</sub> O <sub>4</sub>	→	Si <sub>2</sub> O <sub>2</sub> +Si <sub>2</sub> O <sub>2</sub>	$9.9000 \times 10^{-4}$	0	0	”
A13	Si <sub>5</sub> O <sub>5</sub>	→	Si <sub>3</sub> O <sub>3</sub> +Si <sub>2</sub> O <sub>2</sub>	$9.9000 \times 10^{-4}$	0	0	”
Forsterite (Mg <sub>4</sub> Si <sub>2</sub> O <sub>8</sub> ) and Enstatite (Mg <sub>2</sub> Si <sub>2</sub> O <sub>6</sub> ) dimers							
B1	Si <sub>2</sub> O <sub>2</sub> +O <sub>2</sub>	→	Si <sub>2</sub> O <sub>3</sub> +O	$1.0000 \times 10^{-11}$	0	1000	E
B2	Si <sub>2</sub> O <sub>2</sub> +SO	→	Si <sub>2</sub> O <sub>3</sub> +S	$1.0000 \times 10^{-11}$	0	1000	as B1
B3	Si <sub>2</sub> O <sub>3</sub> +Mg	→	MgSi <sub>2</sub> O <sub>3</sub>	$1.0000 \times 10^{-12}$	0	0	E
B4	MgSi <sub>2</sub> O <sub>3</sub> +O <sub>2</sub>	→	MgSi <sub>2</sub> O <sub>4</sub> +O	$1.0000 \times 10^{-12}$	0	0	as B3
B5	MgSi <sub>2</sub> O <sub>3</sub> +SO	→	MgSi <sub>2</sub> O <sub>4</sub> +S	$1.0000 \times 10^{-12}$	0	0	as B3
B6	MgSi <sub>2</sub> O <sub>4</sub> +Mg	→	Mg <sub>2</sub> Si <sub>2</sub> O <sub>4</sub>	$1.0000 \times 10^{-12}$	0	0	as B3
B7	Mg <sub>2</sub> Si <sub>2</sub> O <sub>4</sub> +O <sub>2</sub>	→	Mg <sub>2</sub> Si <sub>2</sub> O <sub>5</sub> +O	$1.0000 \times 10^{-12}$	0	0	as B3
B8	Mg <sub>2</sub> Si <sub>2</sub> O <sub>4</sub> +SO	→	Mg <sub>2</sub> Si <sub>2</sub> O <sub>5</sub> +S	$1.0000 \times 10^{-12}$	0	0	as B3
B9	Mg <sub>2</sub> Si <sub>2</sub> O <sub>5</sub> +O <sub>2</sub>	→	Mg <sub>2</sub> Si <sub>2</sub> O <sub>6</sub> +O	$1.0000 \times 10^{-12}$	0	0	as B3
B10	Mg <sub>2</sub> Si <sub>2</sub> O <sub>5</sub> +SO	→	Mg <sub>2</sub> Si <sub>2</sub> O <sub>6</sub> +S	$1.0000 \times 10^{-12}$	0	0	as B3
B11	Mg <sub>2</sub> Si <sub>2</sub> O <sub>6</sub> +Mg	→	Mg <sub>3</sub> Si <sub>2</sub> O <sub>6</sub>	$1.0000 \times 10^{-12}$	0	0	as B3
B12	Mg <sub>3</sub> Si <sub>2</sub> O <sub>6</sub> +O <sub>2</sub>	→	Mg <sub>3</sub> Si <sub>2</sub> O <sub>7</sub> +O	$1.0000 \times 10^{-12}$	0	0	as B3
B13	Mg <sub>3</sub> Si <sub>2</sub> O <sub>6</sub> +SO	→	Mg <sub>3</sub> Si <sub>2</sub> O <sub>7</sub> +S	$1.0000 \times 10^{-12}$	0	0	as B3
B14	Mg <sub>3</sub> Si <sub>2</sub> O <sub>7</sub> +Mg	→	Mg <sub>4</sub> Si <sub>2</sub> O <sub>7</sub>	$1.0000 \times 10^{-12}$	0	0	as B3
B15	Mg <sub>4</sub> Si <sub>2</sub> O <sub>7</sub> +O <sub>2</sub>	→	Mg <sub>4</sub> Si <sub>2</sub> O <sub>8</sub> +O	$1.0000 \times 10^{-12}$	0	0	as B3
B16	Mg <sub>4</sub> Si <sub>2</sub> O <sub>7</sub> +SO	→	Mg <sub>4</sub> Si <sub>2</sub> O <sub>8</sub> +S	$1.0000 \times 10^{-12}$	0	0	as B3
Si <sub>n</sub> O <sub>n+1</sub> clusters							
C1	Si <sub>2</sub> O <sub>3</sub> +O	→	Si <sub>2</sub> O <sub>2</sub> +O <sub>2</sub>	$1.0000 \times 10^{-12}$	0	0	E
C4	Si <sub>2</sub> O <sub>3</sub> +S	→	Si <sub>2</sub> O <sub>2</sub> +SO	$1.0000 \times 10^{-12}$	0	0	E
C5	Si <sub>3</sub> O <sub>3</sub> +O <sub>2</sub>	→	Si <sub>3</sub> O <sub>4</sub> +O	$1.0000 \times 10^{-13}$	0	1000	E
C6	Si <sub>3</sub> O <sub>3</sub> +SO	→	Si <sub>3</sub> O <sub>4</sub> +S	$1.0000 \times 10^{-13}$	0	1000	”
C7	Si <sub>4</sub> O <sub>4</sub> +O <sub>2</sub>	→	Si <sub>4</sub> O <sub>5</sub> +O	$1.0000 \times 10^{-13}$	0	1000	”
C8	Si <sub>4</sub> O <sub>4</sub> +SO	→	Si <sub>4</sub> O <sub>5</sub> +S	$1.0000 \times 10^{-13}$	0	1000	”
C9	Si <sub>2</sub> O <sub>3</sub> +SiO	→	Si <sub>3</sub> O <sub>4</sub>	$7.4627 \times 10^{-16}$	0	−2878.9	ZT93
C10	Si <sub>3</sub> O <sub>4</sub> +SiO	→	Si <sub>4</sub> O <sub>5</sub>	$5.0884 \times 10^{-15}$	0	−2386.8	”
C11	Si <sub>2</sub> O <sub>2</sub> +SiO	→	Si <sub>2</sub> O <sub>3</sub> +Si	$7.4627 \times 10^{-16}$	0	−2878.9	”
C12	Si <sub>3</sub> O <sub>3</sub> +SiO	→	Si <sub>3</sub> O <sub>4</sub> +Si	$5.0884 \times 10^{-15}$	0	−2386.8	”
C13	Si <sub>4</sub> O <sub>4</sub> +SiO	→	Si <sub>4</sub> O <sub>5</sub> +Si	$5.0884 \times 10^{-15}$	0	−2386.8	”
Cluster fragmentation							
D1	Si <sub>2</sub> O <sub>2</sub> +M	→	SiO+SiO+M	$4.4000 \times 10^{-10}$	0	98600.0	CD10
D2	Si <sub>3</sub> O <sub>3</sub> +M	→	Si <sub>2</sub> O <sub>2</sub> +SiO+M	$4.4000 \times 10^{-10}$	0	98600.0	”
D3	Si <sub>4</sub> O <sub>4</sub> +M	→	Si <sub>3</sub> O <sub>3</sub> +SiO+M	$4.4000 \times 10^{-10}$	0	98600.0	”
D4	Si <sub>4</sub> O <sub>4</sub> +M	→	Si <sub>2</sub> O <sub>2</sub> +Si <sub>2</sub> O <sub>2</sub> +M	$4.4000 \times 10^{-10}$	0	98600.0	”
D5	Si <sub>5</sub> O <sub>5</sub> +M	→	Si <sub>4</sub> O <sub>4</sub> +SiO+M	$4.4000 \times 10^{-10}$	0	98600.0	”
D6	Si <sub>5</sub> O <sub>5</sub> +M	→	Si <sub>2</sub> O <sub>2</sub> +Si <sub>3</sub> O <sub>3</sub> +M	$4.4000 \times 10^{-10}$	0	98600.0	”
D7	Si <sub>2</sub> O <sub>3</sub> +M	→	Si <sub>2</sub> O <sub>2</sub> +O+M	$5.0000 \times 10^{-10}$	0	55000.0	”
D8	Si <sub>3</sub> O <sub>4</sub> +M	→	Si <sub>3</sub> O <sub>3</sub> +O+M	$5.0000 \times 10^{-10}$	0	55000.0	”
D9	Si <sub>4</sub> O <sub>5</sub> +M	→	Si <sub>4</sub> O <sub>4</sub> +O+M	$5.0000 \times 10^{-10}$	0	55000.0	”
D10	MgSi <sub>2</sub> O <sub>3</sub> +M	→	Si <sub>2</sub> O <sub>3</sub> +Mg+M	$1.0000 \times 10^{-10}$	0	98600.0	as D1
D11	MgSi <sub>2</sub> O <sub>4</sub> +M	→	MgSi <sub>2</sub> O <sub>3</sub> +O+M	$1.0000 \times 10^{-10}$	0	98600.0	”
D12	Mg <sub>2</sub> Si <sub>2</sub> O <sub>4</sub> +M	→	MgSi <sub>2</sub> O <sub>4</sub> +Mg+M	$1.0000 \times 10^{-10}$	0	98600.0	”
D13	Mg <sub>2</sub> Si <sub>2</sub> O <sub>5</sub> +M	→	Mg <sub>2</sub> Si <sub>2</sub> O <sub>4</sub> +O+M	$1.0000 \times 10^{-10}$	0	98600.0	”
D14	Mg <sub>2</sub> Si <sub>2</sub> O <sub>6</sub> +M	→	Mg <sub>2</sub> Si <sub>2</sub> O <sub>5</sub> +O+M	$1.0000 \times 10^{-10}$	0	98600.0	”
D15	Mg <sub>3</sub> Si <sub>2</sub> O <sub>6</sub> +M	→	Mg <sub>2</sub> Si <sub>2</sub> O <sub>6</sub> +Mg+M	$1.0000 \times 10^{-10}$	0	98600.0	”
D16	Mg <sub>3</sub> Si <sub>2</sub> O <sub>7</sub> +M	→	Mg <sub>3</sub> Si <sub>2</sub> O <sub>6</sub> +O+M	$1.0000 \times 10^{-10}$	0	98600.0	”

**Table 10**  
(Continued)

Reaction	Reactants		Products	$A_{ij}$	$\nu$	$E_a$	References <sup>b</sup>
D17	Mg <sub>4</sub> Si <sub>2</sub> O <sub>7</sub> +M	→	Mg <sub>3</sub> Si <sub>2</sub> O <sub>7</sub> +Mg+M	$1.0000 \times 10^{-10}$	0	98600.0	''
D18	Mg <sub>4</sub> Si <sub>2</sub> O <sub>8</sub> +M	→	Mg <sub>4</sub> Si <sub>2</sub> O <sub>7</sub> +O+M	$1.0000 \times 10^{-10}$	0	98600.0	''

**Notes.** A pure chemical kinetic approach has been used whereby the reaction rates are either known (calculated from theory or measured in the laboratory) or estimated. Backward rates are not estimated from detailed balance and thermodynamic data (for more detail, see Cherchneff 2011). The reaction rates are expressed in Arrhenius form and the parameters for each reaction are indicated.

<sup>a</sup> Rates are given in an Arrhenius form  $k = A_{ij} \times (T/300\text{K})^\nu \times \exp(-E_a/T)$  with  $A_{ij}$  in  $\text{s}^{-1}$ ,  $\text{cm}^3 \text{s}^{-1}$ , or  $\text{cm}^6 \text{s}^{-1}$  for uni-, bi- and termolecular processes, respectively;  $E_a$  is in Kelvin.

<sup>b</sup> ZT93  $\equiv$  Zachariah & Tsang (1993); CD10  $\equiv$  Cherchneff & Dwek (2010); E  $\equiv$  Estimated.

**Table 11**  
Compton Electron-induced Reactions, Corresponding Mean Energy per Ion Pair  $W_i$ , and Arrhenius Coefficient A as a Function of Ejecta Model

Species	Reactions	$W_i$ (eV)	<sup>56</sup> Ni = 0.07 $M_\odot$		<sup>56</sup> Ni = 0.01 $M_\odot$			Reference
			A - 15 $M_\odot$ <sup>a</sup>	A - 19 $M_\odot$ <sup>a</sup>	A - 12 $M_\odot$ <sup>a</sup>	A - 15 $M_\odot$ <sup>a</sup>	A - 25 $M_\odot$ <sup>a</sup>	
CO	→ O <sup>+</sup> + C	768	$7.7671 \times 10^{-7}$	$6.1663 \times 10^{-7}$	$4.9768 \times 10^{-7}$	$1.1763 \times 10^{-7}$	$5.6102 \times 10^{-8}$	Liu & Dalgarno (1995)
	→ C <sup>+</sup> + O	247	$2.4150 \times 10^{-6}$	$1.9173 \times 10^{-6}$	$1.5472 \times 10^{-6}$	$3.6576 \times 10^{-7}$	$1.7444 \times 10^{-7}$	''
	→ C + O	125	$4.7722 \times 10^{-6}$	$3.7887 \times 10^{-6}$	$3.0575 \times 10^{-6}$	$7.2268 \times 10^{-7}$	$3.4466 \times 10^{-7}$	''
	→ CO <sup>+</sup> + e <sup>-</sup>	34	$1.7544 \times 10^{-5}$	$1.3928 \times 10^{-5}$	$1.1241 \times 10^{-5}$	$2.6570 \times 10^{-6}$	$1.2672 \times 10^{-6}$	''
O	→ O <sup>+</sup> + e <sup>-</sup>	46.2	$1.2911 \times 10^{-5}$	$1.3082 \times 10^{-5}$	$8.2723 \times 10^{-6}$	$1.9554 \times 10^{-6}$	$9.3259 \times 10^{-7}$	''
C	→ C <sup>+</sup> + e <sup>-</sup>	36.4	$1.6297 \times 10^{-5}$	$1.3010 \times 10^{-5}$	$1.0500 \times 10^{-5}$	$2.4819 \times 10^{-6}$	$1.1837 \times 10^{-6}$	''
SiO	→ O <sup>+</sup> + Si	678	$8.7986 \times 10^{-7}$	$6.9852 \times 10^{-7}$	$5.6372 \times 10^{-7}$	$1.3324 \times 10^{-7}$	$6.3546 \times 10^{-8}$	''
	→ Si <sup>+</sup> + O	218	$2.7363 \times 10^{-6}$	$2.1724 \times 10^{-6}$	$1.7531 \times 10^{-6}$	$4.1441 \times 10^{-7}$	$1.9764 \times 10^{-7}$	''
	→ Si + O	110	$5.4228 \times 10^{-6}$	$4.3051 \times 10^{-6}$	$3.4747 \times 10^{-6}$	$8.2128 \times 10^{-7}$	$3.9169 \times 10^{-7}$	''
	→ SiO <sup>+</sup> + e <sup>-</sup>	30	$1.9884 \times 10^{-5}$	$1.5786 \times 10^{-5}$	$1.2740 \times 10^{-5}$	$3.0114 \times 10^{-6}$	$1.4362 \times 10^{-6}$	''
N <sub>2</sub>	→ N <sup>+</sup> + N	264	$2.2594 \times 10^{-6}$	$1.7938 \times 10^{-6}$	$1.4477 \times 10^{-6}$	$3.4219 \times 10^{-7}$	$1.6320 \times 10^{-7}$	Khare & Kumar (1977)
	→ N + N	133.5	$4.4683 \times 10^{-6}$	$3.5474 \times 10^{-6}$	$2.8628 \times 10^{-6}$	$6.7673 \times 10^{-7}$	$3.2275 \times 10^{-7}$	''
	→ N <sub>2</sub> <sup>+</sup> + e <sup>-</sup>	36.3	$1.6433 \times 10^{-5}$	$1.3046 \times 10^{-5}$	$1.0529 \times 10^{-5}$	$2.4886 \times 10^{-6}$	$1.1870 \times 10^{-6}$	''
He	→ He <sup>+</sup> + e <sup>-</sup>	46.3	$1.2884 \times 10^{-5}$	$1.0229 \times 10^{-5}$	$8.2549 \times 10^{-6}$	$1.9511 \times 10^{-6}$	$9.3054 \times 10^{-7}$	''
Ne	→ Ne <sup>+</sup> + e <sup>-</sup>	36.4	$1.6387 \times 10^{-5}$	$1.3010 \times 10^{-5}$	$1.0500 \times 10^{-5}$	$2.4819 \times 10^{-6}$	$1.1837 \times 10^{-6}$	''
Ar	→ Ar <sup>+</sup> + e <sup>-</sup>	26.2	$2.2767 \times 10^{-5}$	$1.8075 \times 10^{-5}$	$1.4588 \times 10^{-5}$	$3.4481 \times 10^{-6}$	$1.6445 \times 10^{-6}$	''

**Note.** <sup>a</sup> The rate is expressed in an Arrhenius form  $k_C: A \times \exp(-3386.5/T)$ . See Cherchneff & Dwek (2010) for details.

the formation of new grains in the expending ejecta after  $\sim 5$  yr should be hampered by the shortage of the chemical agents responsible for the first nucleation step, i.e., SiO or C<sub>2</sub>, which are depleted in the ejecta between 300 and 2000 days, depending on the progenitor mass. Second, the growth of existing dust grains via accretion of abundant atoms or molecules such as atomic C, Mg, Si, or O<sub>2</sub> on the grain surface will happen on a timescale given by  $\tau_{ac} = [n_d \times \sigma_d \times v \times S(T, T_d)]^{-1}$ , where  $n_d$ ,  $\sigma_d$ , and  $T_d$  are the number density, the collision cross section, and the temperature of the grains, respectively.  $v$  and  $T$  are the thermal velocity and temperature of the gas, respectively, and  $S(T, T_d)$  is the sticking coefficient. For typical grain sizes ( $0.1 \mu\text{m}$ ) and ejecta gas conditions after day 2000 ( $n = 10^6 \text{ cm}^{-3}$  and  $T = 400 \text{ K}$ ), the sticking coefficient is  $\sim 0.5$  and the estimated accretion time  $\tau_{ac}$  is  $\sim 10^4$  yr. This timescale exceeds the free expansion phase of SNe and, by that time, the ejecta will have been reprocessed by the reverse shock in the remnant. Therefore, late grain growth cannot proceed due to the very long accretion time required to add mass to the grains. The dust observed in SNe and SNRs has thus formed in the nebular phase of the ejecta prior to 5 yr after the explosion.

Finally, our finding of a gradual increase in dust mass due to a sequence of various condensation events in the ejecta reconciles the mass values derived from IR data with those

from submm data. A hint of some increase in the dust mass over time was already indicated for SN1987A by Wooden et al. (1993), who inferred a 1.6 factor increase in the dust mass between 615 and 775 days, a value that agrees well with our results for the 19  $M_\odot$  progenitor. Obviously, the present models use simplistic, one-dimensional explosion models for SNe and have not yet included the dust condensation phase. In this regard, three-dimensional explosion models provide more realistic samples of clump chemical compositions. Because of the strong impact of <sup>56</sup>Ni on the ejecta chemistry through the formation of noble gas ions, each clump has a specific composition, thermal, and density history and thus a specific dust condensation scenario and efficiency. Applying a chemical kinetic formalism of the dust synthesis to such clumps, including the thermal feedback of molecules such as CO, SiO, and SiS, will fine-tune the prediction of the final dust mass produced by SN ejecta. However, from the present study, we anticipate that Type II-P SNe are efficient but moderate dust producers in local and remote galaxies. In the context of primeval galaxies at high redshift, the requirement that SNe produce  $\sim 1 M_\odot$  of dust in order to explain the large amount of dust produced at high redshift (Dwek et al. 2007) is not satisfied. According to the present study, the explosion of primitive supergiant stars as SNe should produce at most  $0.1 M_\odot$  of O-rich dust, but grain

destruction induced by shocks in the remnant phase will lower this value. These results argue for alternative and efficient O-rich and carbon dust providers (e.g., asymptotic giant branch stars, quasars) to account for the large dust masses present in the early universe.

We thank the anonymous referee for comments that have contributed to the improvement of the manuscript. We also thank Stefan Bromley, John Plane, Eli Dwek, Rubina Kotak, and Patrice Bouchet for fruitful discussions. A.S. acknowledges support from the Swiss National Science Foundation grant PMPD2-114347 attached to the ESF Eurogenesis network CoDustMas.

## APPENDIX

Two tables are provided in the Appendix. Table 10 lists the chemical scheme and the reaction rates for the nucleation of clusters implicated in the nucleation phase. Table 11 summarizes the rates of reactions with the Compton electrons induced by radioactivity in the ejecta.

## REFERENCES

- Andrews, J., Gallagher, J. S., Clayton, G. C., et al. 2011, *ApJ*, **715**, 541
- Archibong, E. F., & St-Amant, A. 1999, *JPhCh*, **103**, 1109
- Barlow, M. J., Krause, O., Swinyard, B. M., et al. 2010, *A&A*, **518**, L138
- Bertoldi, F., Carilli, C. L., Cox, P., et al. 2003, *A&A*, **406**, 55
- Bianchi, S., & Schneider, R. 2007, *MNRAS*, **378**, 973
- Cherchneff, I. 2010, in ASP Conf. Ser. 425, Hot and Cool: Bridging Gaps in Massive Star Evolution, ed. C. Lietherer, P. Bennett, P. Morris, & J. van Loon (San Francisco, CA: ASP), 237
- Cherchneff, I. 2011, *A&A*, **526**, L11
- Cherchneff, I., & Dwek, E. 2009, *ApJ*, **703**, 642
- Cherchneff, I., & Dwek, E. 2010, *ApJ*, **715**, 1 (CD10)
- Cherchneff, I., & Lilly, S. 2008, *ApJL*, **683**, L123
- Cherchneff, I., & Sarangi, A. 2011, in IAU Symp. 280, The Molecular Universe, ed. J. Cernicharo & R. Bachiller (Cambridge: Cambridge Univ. Press), 228
- Chevalier, R. A., & Kirscher, R. P. 1978, *ApJ*, **219**, 931
- Danziger, I. J., Bouchet, P., Fosbury, R. A. E., et al. 1988, in Proc. Fourth George Mason Astrophysics Workshop, Supernova 1987A in the Large Magellanic Cloud, ed. M. Kafatos & A. Michalitsianos (Cambridge: Cambridge Univ. Press), 37
- Danziger, I. J., Lucy, L. B., Bouchet, P., & Gouffès, C. 1991, in Supernovae, The Tenth Santa Cruz Workshop in Astronomy and Astrophysics, ed. S. E. Woosley (New York: Springer), 69
- Davidson, K., & Fesen, R. A. 1985, *ARA&A*, **23**, 119
- DeLaney, T., Rudnick, L., Stage, M. D., et al. 2010, *ApJ*, **725**, 2038
- Dwek, E., Galliano, F., & Jones, A. P. 2007, *ApJ*, **662**, 927
- Elmhamdi, A., Chugai, N. N., & Danziger, I. J. 2003a, *A&A*, **404**, 1077
- Elmhamdi, A., Danziger, J., Chugai, N. N., et al. 2003b, *MNRAS*, **338**, 939
- Ercolano, B., Barlow, M. J., & Sugerman, B. E. K. 2007, *MNRAS*, **375**, 753
- Fesen, R. A., Hammel, M. C., Morse, J., et al. 2006, *ApJ*, **636**, 859
- Gallagher, J. S., Sugerman, B. E. K., Clayton, G. C., et al. 2012, *ApJ*, **753**, 109
- Gandhi, P., Yamanaka, M., Tanaka, M., et al. 2013, *ApJ*, **767**, 166
- Ghavamian, P., Long, K. S., Blair, W. P., et al. 2012, *ApJ*, **750**, 39
- Gomez, H. L., Krause, O., Barlow, M. J., et al. 2012, *ApJ*, **760**, 96
- Gouman, F., & Bromley, S. T. 2012, *MNRAS*, **420**, 3344
- Hammer, N. J., Janka, H.-Th., & Müller, E. 2010, *ApJ*, **714**, 137
- Hamuy, M. 2003, *ApJ*, **582**, 905
- Hendry, M. A., Smartt, S. J., Maund, J. R., et al. 2005, *MNRAS*, **359**, 906
- Inserra, C., Turatto, M., Pastorello, A., et al. 2011a, *MNRAS*, **417**, 261
- Inserra, C., Turatto, M., Pastorello, A., et al. 2011b, *MNRAS*, **422**, 1122
- Isensee, K., Olmschenk, G., Rudnick, L., et al. 2012, *ApJ*, **757**, 126
- Joggerst, C. C., Almgren, A., & Woosley, S. E. 2010, *ApJ*, **723**, 353
- Kamnetzky, J., McCray, R., Indebetouw, R., et al. 2013, *ApJL*, **773**, L34
- Khare, S. P., & Kumar, A., Jr. 1977, *JPhB*, **10**, 2239
- Kotak, R., Meikle, W. P. S., Farrah, D., et al. 2009, *ApJ*, **704**, 306
- Kotak, R., Meikle, W. P. S., Pozzo, M., et al. 2006, *ApJL*, **651**, L117
- Kotak, R., Meikle, W. P. S., van Dyck, S. D., Höflich, P. A., & Mattila, S. 2005, *ApJL*, **628**, L123
- Kozasa, T., Hasegawa, H., & Nomoto, K. 1989, *ApJ*, **344**, 325
- Kozasa, T., Nozawa, N., et al. 2009, in ASP Conf. Ser. 414, Cosmic Dust—Near and Far, ed. T. Henning, E. Grün, & J. Steinacker (San Francisco, CA: ASP), 43
- Krause, O., Birkmann, S., Usuda, T., et al. 2008, *Sci*, **320**, 1195
- Lepp, S., Dalgarno, A., & McCray, R. 1990, *ApJ*, **358**, 262
- Liu, W., & Dalgarno, A. 1995, *ApJ*, **454**, 472
- Liu, W., Dalgarno, A., & Lepp, S. 1992, *ApJ*, **396**, 679
- Lucy, L. B., Danziger, I. J., Gouffès, C., & Bouchet, P. 1989, in IAU Colloq. 120, Structure and Dynamics of the Interstellar Medium, ed. G. Tenorio-Tagle, M. Moles, & J. Melnick (New York: Springer), 164
- MacAlpine, G. M., & Satterfield, T. J. 2008, *AJ*, **136**, 2152
- Matsuura, M., Dwek, E., Meixner, M., et al. 2011, *Sci*, **333**, 1258
- Mauerhan, J. C., Smith, N. A., Silverman, J. M., et al. 2012, *MNRAS*, **431**, 2599
- Meikle, W. P. S., Spyromilio, J., Varani, G.-F., & Allen, D. A. 1989, *MNRAS*, **238**, 193
- Moseley, S. H., Dwek, E., Glaccum, W., Graham, J. R., & Loewenstein, R. F. 1989, *Natur*, **340**, 697
- Nozawa, T., Kozasa, T., Habe, A., et al. 2010, *ApJ*, **666**, 955
- Nozawa, T., Kozasa, T., Umeda, H., Maeda, K., & Nomoto, K. 2003, *ApJ*, **598**, 785 (NK03)
- Pastorello, A., Valenti, S., Zampieri, L., et al. 2009, *MNRAS*, **394**, 2266
- Pei, Y. C., Fall, S. M., & Bechtold, J. 1991, *ApJ*, **378**, 6
- Pettini, M., Smith, L. J., Hunstead, R. W. M., & King, D. L. 1994, *ApJ*, **426**, 79
- Rauscher, T., Heger, A., Hofmann, R. D., & Woosley, S. E. 2002, *ApJ*, **576**, 323
- Reber, A. C., Paranthaman, S., Clayborne, P. A., et al. 2008, *ACSnano*, **2**, 1729
- Rho, J., Jarrett, T., Reach, W., et al. 2009, *ApJ*, **693**, 39
- Rho, J., Onaka, T., Cami, J., & Reach, W. 2012, *ApJ*, **747**, 6
- Roche, P. F., Aitken, D. K., & Smith, C. H. 1991, *MNRAS*, **252**, 39
- Sibthorpe, B., Ade, P. A. R., & Bock, J. J. 2010, *ApJ*, **719**, 1553
- Smartt, S. J. 2009, *ARA&A*, **47**, 63
- Smartt, S. J., Maund, J. R., Hendry, M. A., et al. 2004, *Sci*, **303**, 499
- Spyromilio, J., Meikle, W. P. S., Learner, R. C. M., & Allen, D. A. 1988, *Natur*, **334**, 327
- Sugerman, B. E. K., Ercolano, B., Barlow, M. J., et al. 2006, *Sci*, **313**, 196
- Tielens, A. G. G. M., Waters, L. B. F. M., Molster, F. J., & Justtanont, K. 1998, *Ap&SS*, **255**, 415
- Todini, P., & Ferrara, A. 2001, *MNRAS*, **325**, 726
- Tumlinson, J. 2006, *ApJ*, **641**, 1
- Vinkó, J., Sárneczky, K., Balog, Z., et al. 2009, *ApJ*, **695**, 619
- Wang, X., Yang, Y., Zhang, T., et al. 2005, *ApJL*, **626**, L89
- Wooden, D. H., Rank, D. M., Bregman, J. D., et al. 1993, *ApJS*, **88**, 477
- Woosley, S. E. 1988, *ApJ*, **320**, 218
- Woosley, S. E., & Heger, A. 2007, *PhR*, **442**, 269
- Zachariah, M. R., & Tsang, W. 1993, *AerST*, **19**, 499 (ZT93)